Hunt, G. , Karimi, N. , Yadollahi, B. and Torabi, M. (2019) The effects of exothermic catalytic reactions upon combined transport of heat and mass in porous microreactors. *International Journal of Heat and Mass Transfer*, 134, pp. 1227-1249. (doi: 10.1016/j.ijheatmasstransfer.2019.02.015)

The effects of exothermic catalytic reactions upon combined transport of heat and mass in porous microreactors

Graeme Hunt [a], Nader Karimi[1][a], Bijan Yadollahi [a], Mohsen Torabi [b,c]

[a] School of Engineering, University of Glasgow, Glasgow G12 8QQ, United Kingdom
[b] The George W. Woodruff School of Mechanical Engineering, Georgia Institute of Technology, Atlanta, GA 30332, USA
[c] School of Engineering, University of California, Merced, CA 95348, USA

Abstract

Microreactors for chemical synthesis and combustion have already attracted significant attention. Exothermic catalytic activity features heavily in these devices and thus advective-diffusive transport is of key importance in their analyses. Yet, thermal modelling of the heat generated by catalytic reactions on the internal surfaces of porous microreactors has remained as an important unresolved issue. To address this, the diffusion of heat of catalytic reactions into three phases including fluid, porous solid and solid walls is investigated by extending an existing interface model of porous media under local thermal non-equilibrium. This is applied to a microchannel fully filled with a porous material, subject to a heat flux generated by a catalytic layer coated on the porous-wall boundary. The finite wall thickness and viscous dissipation of the flow kinetic energy are considered, and a two-dimensional analytical model is developed, examining the combined heat and mass transfer and thermodynamic irreversibilities of the system. The analytical solution is validated against the existing theoretical studies on simpler configurations as well as a computational model of the microreactor in the limit of very large porosity. In keeping with the recent findings, the wall thickness is shown to strongly influence the heat and mass transport within the system. This remains unchanged when the symmetricity of the microchannel is broken through placing walls of unequal thicknesses, while deviation from local thermal equilibrium is significantly intensified in this case. Importantly, the Nusselt number is shown to have a singular point, which remains fixed under various conditions.

Keywords: Microreactors; Local thermal non-equilibrium; Surface heat release; Soret effect; Double-diffusive; Entropy generation.

Nomenclature

a_{sf}	Interfacial area per unit volume of porous media, (m^{-1})	Pr	Prandtl number
Bi	Biot number	Q	Wall heat flux ratio
Br'	Modified Brinkman number	q_c''	Total catalytic heat flux (W m^{-2})
C	Mass species concentration (kg m^{-3})	q_{w1}''	Lower wall heat flux (W m^{-2})
C_0	Inlet concentration (kg m^{-3})	q_{w2}''	Upper wall heat flux (W m^{-2})
C_p	Specific heat capacity (J K^{-1} kg^{-1})	Re	Reynolds number
D	Mass diffusion coefficient (m^2 s^{-1})	R	Specific gas constant (J K^{-1} kg^{-1})
Da	Darcy number	S	Shape factor of the porous medium
D_T	Coefficient of thermal mass diffusion (m K^{-1} kg^{-1} s^{-1})	$\dot{S}_{Di}'''$	Volumetric entropy generation due to mass diffusion (W K^{-1} m^{-3})
h_1	Half-thickness of the microchannel to lower wall (m)	$\dot{S}_{FF}'''$	Volumetric entropy generation due to fluid friction (W K^{-1} m^{-3})
h_2	Half-thickness of the microchannel to upper wall (m)	$\dot{S}_f'''$	Volumetric entropy generation in the fluid (W K^{-1} m^{-3})
h_3	Half-height of microchannel (m)	$\dot{S}_s'''$	Volumetric entropy generation in the porous solid (W K^{-1} m^{-3})
h_{sf}	Interstitial heat transfer coefficient (W K^{-1} m^{-2})	$\dot{S}_1'''$	Volumetric entropy generation rate from lower wall (W K^{-1} m^{-3})

---

[1] Corresponding author: Nader.Karimi@glasgow.ac.uk

H_w	Wall heat transfer coefficient (W K^{-1} m^{-2})	$\dot{S}_2'''$	Volumetric entropy generation rate from upper wall (W K^{-1} m^{-3})
k	Effective thermal conductivity ratio of the fluid and the porous solid	Sr	Soret number
k_1	Thermal conductivity of wall 1 (W K^{-1} m^{-1})	T	Temperature (K)
k_2	Thermal conductivity of wall 2 (W K^{-1} m^{-1})	u	Fluid velocity (m s^{-1})
k_{e1}	Ratio of thermal conductivity of wall 1 and thermal conductivity of the porous solid	$\bar{u}$	Average velocity over cross-section (m s^{-1})
k_{e2}	Ratio of thermal conductivity of wall 2 and thermal conductivity of the porous solid	x	Dimensional axial coordinate
k_{ef}	Effective thermal conductivity of the fluid phase (W K^{-1} m^{-1})	X	Dimensionless axial coordinate
k_{es}	Effective thermal conductivity of the solid phase of the porous medium (W K^{-1} m^{-1})	y	Dimensional transverse coordinate
k_R	Reaction rate constant on the walls (m s^{-1})	Y	Dimensionless transverse coordinate
L	Length of the microchannel (m)		*Greek symbols*
M	Viscosity Ratio	μ	Dynamic viscosity (N s m^{-2})
N_{DI}	Dimensionless diffusive irreversibility	κ	Permeability (m^2)
N_{FF}	Dimensionless fluid friction irreversibility	ρ	Density (kg m^{-3})
N_{int}	Dimensionless interstitial heat transfer irreversibility	θ	Dimensionless temperature
N_f	Dimensionless fluid and interstitial irreversibility	Φ	Dimensionless concentration
$N_{f,ht}$	Dimensionless fluid heat transfer irreversibility	ξ	Aspect ratio of the microchannel
N_s	Dimensionless porous solid and interstitial irreversibility	ε	Porosity of the porous medium
$N_{s,ht}$	Dimensionless heat transfer irreversibility	γ	Damköhler number
N_1	Dimensionless lower wall irreversibility	ω	Dimensionless heat flux defined in Eq. (42)
N_2	Dimensionless upper wall irreversibility	φ	Irreversibility distribution ratio defined in Eq. (43)
N_{pm}	Dimensionless total porous medium irreversibility		*Temperature Subscripts*
N_{Tot}	Dimensionless total entropy	f	Fluid
Nu	Nusselt number	s	porous solid
p	Pressure (Pa)	1	lower wall
Pe	Peclet number	2	upper wall

1. Introduction

Recent years have seen a surge of interest in microreactors for applications in a diverse range of technologies. Microreactors often consist of several tubular or planar microchannels that host chemically reactive flows. The reactions can be either homogenous and occur throughout the fluid or heterogeneous and take place on the surface a catalyst. Due to the small characteristic lengths, as compared to reactors on the macro scale, the diffusion of heat and mass occurs far more efficiently in microreactors [1]. In addition, the high area to volume ratio permits efficient transport [2]. Further thermal performance enhancement can be accomplished by filling the microchannel with a porous material [3–5]. This permits a high degree of control upon the thermal conditions within the microreactor in addition to a very efficient mixing of reactants, which enables a greater degree of selectivity as compared to traditional reactors [6,7]. As such, microreactors are of interest for chemical synthesis [1,8,9] and are particularly suited to highly exothermic and endothermic reactions [5,10,11]. Experimental investigations of transport in microreactors have been conducted and comparisons have been made with the numerical analyses [12–14]. In particular, the enclosing structure (thick walls of the microreactor) was found to have significant impacts upon the performance of microreactors [15–17].

As opposed to classical reaction vessels, where the vessel walls comprise a relatively small component of the total volume of the system, the walls of a microchannel are of comparable volume to that of the microchannel itself. Recent studies of microreactors have revealed the essential necessity of taking into account the enclosing structure when examining the transport of heat [18,19] and mass [17]. It is common for microreactors to feature multiple microchannels inside which chemical reactions take place [5,8]. Although in conventional macro-reactors the relatively thin walls have little effect and hence may be reasonably neglected, this is clearly not the case for microreactors [18–20]. In fact, it has been already shown that the solid thick walls can have significant effects upon heat transfer in microchannels [21–23]. The relationship between enclosing structure and the Nusselt number has been demonstrated analytically in both one-dimensional [18] and two-dimensional cases [16,17]. Further, the thermal field influences the thermo-diffusion of mass and therefore makes it subject to effects related to wall thickness.

Porous inserts have been repeatedly used for heat transfer enhancement in microchannels, rendering them an essential part of thermal analysis of many microreactors. In general, low heat exchanges between the fluid and porous solid phase [24], internal heat generations [25,26] and short lengths of flow conduits [27] can cause deviation from local thermal equilibrium (LTE) and necessitate local thermal non-equilibrium (LTNE) analysis. Importantly, almost all these effects are likely to exist in microreactors. Further, viscous dissipation causes a considerable increase in the temperature of the fluid due to conversion of kinetic energy to thermal energy, presenting another route through which the fluid and solid phases of the porous medium may differ. In macro devices and under forced convection, viscous dissipation effects are often omitted. However, due to the greater length to diameter ratio in the micro-systems, the effects of viscous dissipation are appreciable [28]. It has been demonstrated that for fluid flow in microchannels with hydraulic diameters less than 100μm, the viscous dissipation cannot be neglected without inducing significant error [29–31].

Mass transfer analyses in microreactors often follow Fick's law to provide analytical solutions for the advection-diffusion equations [1,32,33]. Thermo-diffusive coupled effects have been additionally examined in a porous microchannel with a catalytic internal surface on the walls by Matin and Pop [34]. These authors investigated the one-dimensional diffusion of mass with Soret effect using a nanofluid under LTE conditions of heat transfer with the wall thickness neglected [34]. Most recently, two-dimensional heat and mass transfer in porous microreactors under LTNE conditions was investigated through including the thermal diffusion of mass (the Soret effect) [16,17]. In the case where the reaction is homogeneous the effects of decreasing thickness of the enclosing structure decreased the local temperature of the fluid phase and in turn the concentration field due to the effect of thermal diffusion [16]. It was argued that in the presence of strong temperature gradient the Soret effect could be quite noticeable, which highlights the significance of accurate thermal analysis for achieving improved mass transfer predictions [17]. It is therefore expected that mass transfer analysis of microreactors accommodating exothermic catalytic reactions requires a detailed heat transfer study.

Second law analysis of microreactors detects areas for possible performance enhancement [35] by leading to the understanding of the destruction of exergy. Recent works have begun to pave the way for the entropy generation analysis of microchannels and thereby for microreactors [18,19,36]. The conventional one-dimensional approach to the problem of entropy generation in microchannels was extended to two-dimensional analysis by Ting et al. [37,38] in their investigations of a fully filled porous microchannel. The investigations assumed LTNE and took into account viscous dissipation effect and heat sources within the fluid. The authors separated the

contributions of local entropy generation from different sources and compared the irreversibilities from each source. In keeping with other authors [18,27,39,40], Ting et al. emphasised the necessity to consider LTNE when there are heat source/sinks in the system. The investigations of Ting et al. [37,38] did not include thick walls. Such examination was conducted by Hunt et al. [16,17] who considered a case with symmetric structure enclosing a fully filled porous microchannel under LTNE conditions. They examined the local entropy contributions in a similar manner as Ting et al. [38] with the addition of a contribution of the concentration field. Interestingly, it was shown that for most cases the contribution by the concentration field dominated the local entropy field by orders of magnitude [17].

The preceding review of literature shows that analytical modelling of transport and thermodynamic irreversibilities in porous microchannels have been now extended to LTNE and two-dimensional analyses [37,38]. The studies in reactive systems have included homogeneous [16] and heterogeneous [17] reactions and investigated combined transport of heat and mass and entropy generation. However, exothermic catalytic reactions have been excluded from these investigations. This is, in part, due to the mathematical difficulties associated with consideration of heat release on the internal surfaces of a microchannel. More importantly, the lack of an LTNE interface model capable of considering the wall, fluid and porous solid collectively has rendered the thermal analyses of such systems impossible. The current work tackles these challenges through developing an analytical model of heat and mass transfer in a porous, thick-wall microreactor with exothermic catalytic reactions occurring on the internal surfaces of the walls. Towards this aim, an existing model of porous interface is extended to include the wall effects.

2.   Analytical methods
2.1 Model concept, configuration and assumptions

The simplest way to examine the boundary between the walls and the porous medium is by treating the fluid phase and porous matrix as a homogeneous medium [41,42], assuming that both phases are at equal temperatures. This is known as the one-equation or LTE model. A more detailed, and accurate, approach is taken by the LTNE model, which treats the solid and fluid phases as separate entities with explicit thermal properties [43]. Thus, two energy equations are required, one for each phase of the porous medium. The heat flux is then split based on the thermal conductivities of the respective phases of the porous material and the corresponding temperature gradients. Splitting the heat flux in this manner is referred to as Model A [25,44–46] and has been widely used in literature (see for example [39,40,47,48]). In enacting this procedure, the effective thermal conductivity of each phase is used. At the interface between the porous medium and the channel wall, parts of the wall are in contact with the fluid phase of the porous medium and other parts are in contact with the porous solid phase. Model A determines the share of each phase from the interface heat flux based on the following expression [44,45],

$$q_{interface} = k_{es} \left. \frac{\partial T_s}{\partial y} \right|_{interface} + k_{ef} \left. \frac{\partial T_f}{\partial y} \right|_{interface}.$$

Other variations of this LTNE model have also been examined with a view to taking into account other effects such as variable porosity and thermal dispersion [44]. Extensive examination of these models revealed that, for many cases, Model A can represent the interface condition with the greatest accuracy [44]. Importantly, however, Model A assumes that the wall in contact with the porous medium is of zero thickness and is therefore unable to conduct heat. For this reason, Model A cannot be used in analysis of heat release on the internal surface of thick

walls facing a porous medium, a situation frequently encountered in catalytic microreactors. Hence, specific interface models should be developed for this particular problem.

Figure 1 shows schematically the system under investigation including two dissimilar thick walls, the internal surface of which coated with catalysts enhancing exothermic reactions. The heat generated by this reaction imposes a constant heat flux, which is applied to the wall (to which the catalyst is adhered), also to the porous medium. A theoretical heat and mass transfer analysis is conducted through making the following assumptions.

- The analysis is macroscopic and based on the general theory of local thermal non-equilibrium and thus pore-scale phenomena are not considered.
- In keeping with the previous theoretical analyses of catalytic reactions in microchannels [34,49,50], the catalyst is assumed to be located on the internal surfaces of the microchannel. Further, the reaction is not diffusion controlled such that diffusive flux of species produced on the surface of the catalyst is at least equal to the rate of species production.
- The pore-scale Reynolds number is assumed to be less than one [42], while the Reynolds number used in this investigation is based on the microchannel height.
- The problem is generally asymmetric and thus the microchannel wall thicknesses and the heat releases on the catalytic surfaces can be uneven.
- Processes featuring abrupt reaction zones, separating hot and cold flows, such as those in micro-combustors [51,52] are not considered here. As a result, the axial conduction of heat within the walls is insignificant and is neglected throughout the analysis [53]. This is further justified by noting that experimental studies [53] have already shown that the axial temperature gradient within the enclosing structure diminishes in thick wall microreactors.

Further, thermo-diffusive mass transfer is examined in the form of the Soret effect. The dependence of the sign of Soret number upon the relative size of the diffusive molecules and the base fluid is considered in the formulation of the advective-diffusive equation. Viscous dissipative effects are also included in the thermal analysis. These terms represent the heat generated from fluid friction and the term associated with the mechanical power actually required to force the fluid through the porous medium. Further assumptions are made in the following section.

2.2 Governing equations and boundary conditions

2.2.1 Momentum transport

The transport of momentum acting under the assumptions that the incompressible fluid flow is steady and laminar satisfying the no-slip boundary conditions on the wall. The flow is from left to right as shown in Figure 1 and is in the axial direction only. Under steady state and for a fully developed flow, Darcy-Brinkman momentum equation governs the hydrodynamics of the system [54]. That is

$$-\frac{\partial p}{\partial x} + \mu_{eff}\frac{d^2 u}{dy^2} - \frac{\mu_f}{\kappa}u = 0, \qquad\qquad -h_1 \leq y < h_2 \qquad (1)$$

where μ_f and μ_{eff} are the viscosity of the fluid and the effective viscosity of the porous medium respectively, u is the velocity of the fluid phase, κ is the permeability of the porous insert, $\frac{\partial p}{\partial x}$ is the pressure gradient and y is the radial direction as determined from the centre plane bisecting the microchannel for reference purposes (see Fig. 1). This equation applies to the porous region, and has a range of the interface between the porous medium and Wall 1, (at $-h_1$) and the interface between the porous medium and Wall 2 (at h_2).

The no-slip boundary conditions on the microchannel walls are:

$$y = h_2: \qquad\qquad\qquad\qquad u = 0 \qquad\qquad\qquad\qquad\qquad (2a)$$

$$y = -h_1: \qquad\qquad\qquad\qquad u = 0 \qquad\qquad\qquad\qquad\qquad (2b)$$

2.2.2 Mass Transport

The chemical reactions are limited to a zeroth-order reversible, catalytic reaction taking place over a catalyst situated upon the walls of the porous channel as shown in Fig. 1. The catalyst is assumed to be unaffected by temperature [34] and heat releases on the catalytic surfaces can be uneven. Further, diffusive flux of species produced on the surface of the catalyst is at least equal to the rate of species production. Using the following advective-diffusive model, transfer of chemical species by taking into account transport due to the Soret effect as well as diffusion of species [33] can be described.

$$u \frac{\partial C}{\partial x} = D \frac{\partial^2 C}{\partial y^2} - D_T \frac{\partial^2 T_f}{\partial y^2}. \qquad\qquad -h_1 \leq y < h_2 \qquad (3)$$

Here, C is the concentration and D is the mass diffusion coefficient. The subtraction of the second derivative of fluid temperature in Eq. (3) arises from the dependence of the sign of Soret number upon the relative size of the diffusive molecules and the base fluid [33]. Here, a negative sign in front of a positive thermodiffusion coefficient, D_T expresses negative Soret number.

The boundary conditions associated with the mass transfer, Eq. (3), are given in expressions (4). The reference value C_0 is the concentration on the lower wall at the entrance to the considered section of the microchannel. This leads to the second imposed condition:

$$y = \frac{h_2 - h_1}{2}: \qquad\qquad\qquad D \frac{\partial C}{\partial y} = D_T \frac{\partial T_f}{\partial y} \qquad\qquad (4a)$$

$$C(0, -h_1): \qquad\qquad\qquad\qquad C = C_0 \qquad\qquad\qquad\qquad (4b)$$

It is noted that the mass transfer model developed in this section serves as a rough approximation of the complex mass transfer phenomena occurring in catalytic microreactors.

2.2.3 Energy transport

The axial conduction of heat within the walls is insignificant and is neglected in this study [53]. Transfer of heat in Wall 2, where k_2 and T_2 are the temperature and thermal conductivity ratio of Wall 2 respectively, is governed by;

$$k_2 \frac{\partial}{\partial y}\left[\frac{\partial T_2}{\partial y}\right] = 0 \qquad\qquad\qquad h_2 < y \leq h_3 \qquad (5a)$$

The porous medium is homogenous, isotropic and fluid saturated and is under LTNE. In addition, gravitational effects and radiative heat transfer are ignored. Physical properties such as porosity, specific heat, density and thermal conductivities are invariants and thermal dispersion effects are ignored. Fully developed thermal flow is assumed. The local thermal non-equilibrium condition assumed for energy equation within the solid and fluid phases of the porous media are expressed by the followings [18,38], while viscous dissipation effects are included.

$$k_{ef} \frac{\partial^2 T_f}{\partial y^2} + h_{sf} a_{sf}\left(T_s - T_f\right) + \frac{\mu_f}{\kappa} u^2 + \mu_{eff}\left(\frac{du}{dy}\right)^2 = \rho_f C_{p,f} u \frac{\partial T_f}{\partial x} \qquad -h_1 \leq y < h_2 \qquad (5b)$$

6

$$k_{es}\frac{\partial^2 T_s}{\partial y^2} - h_{sf}a_{sf}\left(T_s - T_f\right) = 0, \qquad\qquad -h_1 \leq y < h_2 \qquad (5c)$$

In these equations, k_{ef} and T_f are the temperature and effective thermal conductivity of the fluid phase of the porous medium, respectively. Similarly, k_{es} and T_s are the temperature and effective thermal conductivity of the solid phase of the porous medium respectively. The interstitial heat transfer coefficient is represented by h_{sf} and the specific surface area by a_{sf}, while ρ_f is the fluid density and $C_{p,f}$ is the fluid specific heat capacity.

For Wall 1 the energy equation is;

$$k_1\frac{\partial}{\partial y}\left[\frac{\partial T_1}{\partial y}\right] = 0, \qquad\qquad -h_3 \leq y < -h_1 \qquad (5d)$$

in which k_1 and T_1 are the temperature and thermal conductivity ratio of Wall 1, respectively. The equations of heat transfer throughout the microchannel are subject to the following boundary conditions [18,38]:

At the outer edge of Wall 2, the heat flux, q_{w2}'' (see Fig. 1) is defined as follows;

$$y = h_3: \qquad k_2\frac{\partial T_2}{\partial y}\bigg|_{y=h_3} = -q_{w2}''. \qquad\qquad (6a)$$

where the porous medium meets Wall 2, the interface requires a constant temperature condition between the phases of the porous medium and the wall itself. In addition, the heat flux from the catalytic surface q_c'' is split into these respective phases on the basis of their effective thermal conductivities and temperature gradients.

$$y = h_2: \qquad T_2 = T_f = T_s, \qquad q_c'' = k_{ef}\frac{\partial T_f}{\partial y}\bigg|_{y=h_2} + k_{es}\frac{\partial T_s}{\partial y}\bigg|_{y=h_2} - k_2\frac{\partial T_2}{\partial y}\bigg|_{y=h_2} \qquad (6b)$$

Similarly for the interface between the porous medium and Wall 1:

$$y = -h_1: \qquad T_1 = T_f = T_s, \qquad q_c'' = -k_{ef}\frac{\partial T_f}{\partial y}\bigg|_{y=-h_1} - k_{es}\frac{\partial T_s}{\partial y}\bigg|_{y=-h_1} + k_1\frac{\partial T_1}{\partial y}\bigg|_{y=-h_1} \qquad (6c)$$

Finally, at the outer edge of Wall 1, the heat flux, q_{w1}'' (see figure 1) is defined as;

$$y = -h_3: \qquad k_1\frac{\partial T_1}{\partial y}\bigg|_{y=-h_3} = q_{w1}'' \qquad\qquad (6d)$$

Equations (6b) and (6c) are extensions of the well-known Model A of Vafai and his co-workers [44,46]. Model A assumes that the split of heat flux on the interface of the porous insert occurs on the basis of the thermal conductivity and transversal temperature gradients of the solid and fluid phases. Thus, a logical extension of this model, for the configuration shown in Fig. 1, is to add the product of wall thermal conductivity and vertical temperature gradient to those of fluid and porous solid. This permits the total heat flux output of the catalyst, $q_{c,}''$ to be split into its respective heat fluxes into the wall and porous medium. The validity of this extension will be demonstrated later.

2.2.4 Dimensionless Parameters

In order to solve the governing equations, it is necessary to render them dimensionless. This is accomplished by defining a series of dimensionless parameters. The parameters listed in Table 1 are introduced to enable further physical analysis.

Table 1. Definition of dimensionless parameters

$\theta_i = \dfrac{(T_i - T_{w,in})k_{es}}{(q_1'' + q_2'')h_3}$,	$u_r = -\dfrac{h_3^2}{\mu_f}\dfrac{\partial p_f}{\partial x}$,	$Bi = \dfrac{h_{sf} a_{sf} h_3^2}{k_{es}}$,	$\gamma = \dfrac{k_R(h_1 + h_2)}{D C_0}$,
$Y = \dfrac{y}{h_3}$,	$Da = \dfrac{\kappa}{h_3^2}$,	$Br' = \dfrac{\mu_{eff}\bar{u}^2}{(q_1'' + q_2'')h_3}$,	$Sr = \dfrac{(q_1'' + q_2'')(h_1 + h_2)D_T}{C_0 k_f D}$,
$Y_1 = \dfrac{h_1}{h_3}$,	$M = \dfrac{\mu_{eff}}{\mu_f}$,	$k_{e1} = \dfrac{k_1}{k_{es}}$,	$Q = \dfrac{q_2''}{(q_1'' + q_2'')}$,
$Y_2 = \dfrac{h_2}{h_3}$,	$S = \dfrac{1}{\sqrt{MDa}}$,	$k_{e2} = \dfrac{k_2}{k_{es}}$,	$k = \dfrac{k_{ef}}{k_{es}} = \dfrac{\varepsilon k_f}{(1 - \varepsilon)k_s}$,
$\xi = \dfrac{h_3}{L}$,	$Pr = \dfrac{C_{p,f}\mu_{eff}}{k_{ef}}$,	$\Phi = \dfrac{C}{C_0}$,	$Re = \dfrac{h_3 \rho_f \bar{u}}{\mu_{eff}}$,
$U = \dfrac{u}{u_r}$,	$Pe = \dfrac{\bar{u}(h_1 + h_2)}{D}$,	$Q_{w1} = \dfrac{q_{w1}''}{(q_1'' + q_2'')}$,	$Q_{w2} = \dfrac{q_{w2}''}{(q_1'' + q_2'')}$,
$X = \dfrac{x}{L}$,	$q_1'' = q_c'' - q_{w1}''$,	$q_2'' = q_c'' - q_{w2}''$	

In Table 1 the temperature follows the labelling convention; i= 1, 2, *s, f.*

3. Model development

Equation (1) can be non-dimensionalised using the parameters defined in Table 1. The outcome is the governing equation for the non-dimensional velocity, U with respect to the radial component in dimensionless form, Y, which reads

$$M\frac{d^2 U}{dY^2} - \frac{U}{Da} + 1 = 0. \qquad\qquad -Y_1 \le Y < Y_2 \qquad (7)$$

In Eq. (7), Da is the Darcy number (see Table 1). It is common practice to assume that $\mu_{eff} = \mu_f$ as it has been shown to yield acceptable results [55]. This leads to $M = 1$, where M is the viscosity ratio (see Table 1), and thus shape factor of the porous medium, $S = \frac{1}{\sqrt{Da}}$ [54,56]. Similarly, the no-slip boundary condition expressed in non-dimensional form is:

$$U(\pm Y_1) = 0, \qquad\qquad (8)$$

The solution of Eq. (7) yields;

$$U(Y) = A_1 \cosh(SY) + A_2 \sinh(SY) + Da \qquad\qquad -Y_1 \le Y < Y_2 \qquad (9)$$

Using Eq. (9), the average dimensionless velocity across the microchannel is found to be:

$$\bar{U} = \frac{DaS(Y_1 + Y_2) + A_1(\sinh(SY_1) + \sinh(SY_2)) + A_2(\cosh(SY_2) - \cosh(SY_1))}{S(Y_1 + Y_2)}. \qquad (10)$$

By combining Eqs. (9) and (10) the following ratios are defined;

$$u/\bar{u} = U/\bar{U} = A_3(Da + A_1 \cosh(SY) + A_2 \sinh(SY)). \qquad\qquad (11)$$

8

The constants A_1 to A_3 along with all other constants used henceforth are defined explicitly in Appendix A. Due to the assumption of fully developed flow and by considering the assumptions summarised in section 2, the following conditions hold [38],

$$\frac{\partial T_f}{\partial x} = \frac{d\bar{T}_f}{dx} = \frac{\partial T_s}{\partial x} = \frac{d\bar{T}_s}{dx} = \frac{dT_{w1}}{dx} = \frac{dT_{w2}}{dx} = \Omega = \text{constant.} \tag{12}$$

This permits seeking a solution for the temperature equations of the form:

$$T_i(x, y) = f_i(y) + \Omega x \qquad i = 1, 2, s, f, \tag{13}$$

where $f_i(y)$ is a function to be determined by solving Eqs. (5a) to (5d) and applying the boundary conditions detailed in Eqs. (6a) to (6d). Determination of solutions to the transports of thermal energy equations within the porous microchannel requires the addition of Eqs. (5b) and (5c) in the first instance. The resulting equation is then integrated over the cross-section of the asymmetric microchannel. Substituting into the heat flux boundary conditions from Eqs. (6b) and (6c) and utilising the heat flux relationships stated in Table 1 gives rise to

$$q_1'' + q_2'' + \frac{\mu_{nf}}{\kappa} \int_{-h_1}^{h_2} u^2 \, dy + \mu_{eff} \int_{-h_1}^{h_2} \left(\frac{du}{dy}\right)^2 dy = \rho_f C_{p,f} \int_{-h_1}^{h_2} u \frac{\partial T_f}{\partial x} \, dy. \tag{14}$$

Rearranging Eq. (11) allows substitution for u in Eq. (14). Conversion to non-dimensional parameters as defined in Table 1 simplifies integration, which yields:

$$\frac{d\bar{T}_f}{dx} = \frac{\left[2h_3(q_1'' + q_2'') + \mu_{eff}\bar{u}^2 A_4\right]}{(\rho_f C_{p,f})\bar{u}(h_1 + h_2)h_3} = \Omega, \tag{15}$$

where the bulk mean temperature of the fluid is given by:

$$\bar{T}_f = \frac{1}{\bar{u}(h_1 + h_2)} \int_{-h_1}^{h_2} u T_f \, dy. \tag{16}$$

The axial temperature distribution may now be determined by applying Eq. (12) to Eq. (15) followed by non-dimensionalising the resulting differential equation. Solving the resultant equation such that the solution satisfies Eq.(13) yields the dimensionless temperature, θ_i in the non-dimensional axial direction, X:

$$\theta_i(X) = \frac{X\left[1 + Br'A_4\right]}{Re \, Pr \, k \, (Y_1 + Y_2)\xi}, \qquad i = 1, 2, s, f \tag{17}$$

where Br', Re, Pr, ξ are the modified Brinkman number representing the ratio of the heat produced by viscous dissipation to the heat transferred by conduction, the Reynolds number, Prandtl number, and the aspect ratio of the microchannel, respectively. Further, k is the ratio of the effective fluid to effective solid thermal conductivity as defined in Table 1.

Non-dimensional forms of Eqs. (6a-d) are obtained through algebraic manipulation and by substitution of the parameters listed in Table 1 and application of Eqs. (12) and (15) to give dimensionless energy equation at Wall 2. That is

$$k_{e2}\theta_2'' = 0 \qquad\qquad\qquad Y_2 < Y \le 1 \tag{18a}$$

Dimensionless energy equations in the porous medium are expressed by

$$k\theta_f'' + Bi(\theta_s - \theta_f) + B_1 \cosh(2SY) + B_2 \sinh(2SY) + B_3 \cosh(SY) \qquad -Y_1 \le Y < Y_2 \tag{18b}$$
$$+ B_4 \sinh(SY) + B_5 = 0,$$

$$\theta_s'' - Bi(\theta_s - \theta_f) = 0, \qquad\qquad\qquad\qquad -Y_1 \le Y < Y_2 \tag{18c}$$

where Bi is the Biot number as defined in Table 1. Dimensionless energy equation in Wall 1reads;

$$k_{e1}\theta_1'' = 0 \qquad\qquad\qquad -1 \leq Y < -Y_1 \quad (18d)$$

Differentiation of Eqs (18b) and (18c), allows for the decoupling of these equations resulting in:

$$k\theta_f'''' - \alpha^2\theta_f'' + (4S^2 - Bi)B_1\cosh(2SY) + (4S^2 - Bi)B_2\sinh(2SY) \qquad\qquad (19a)$$
$$+ (S^2 - Bi)B_3\cosh(SY) + (S^2 - Bi)B_4\sinh(SY) - BiB_5 = 0,$$

$$k\theta_s'''' - \alpha^2\theta_s'' - Bi[B_1\cosh(2SY) + B_2\sinh(2SY) + B_3\cosh(SY) + B_4\sinh(SY) + B_5] = 0, \qquad (19b)$$

where $\alpha = \sqrt{Bi(1 + k^{-1})}$.

Once Eqs. (6a) to (6d) have been rendered dimensionless, along with Eqs. (18b) and (18c) the eight boundary conditions of the two fourth order differential Eqs. (19a) and (19b) can be defined. Four boundary conditions are further required in order to solve Eqs. (18a) and (18d), which are themselves linked to Eqs. (19a) and (19b) by the virtue of thermal relationships in the system under investigation. Eqs. (6a to 6d) provide the necessary extra boundary conditions. This concludes the 12 boundary conditions required for the closure of the system, which read as summarised in Table 2.

Table 2. Boundary conditions for closure of the system.

$\theta_f(-Y_1) = \theta_s(-Y_1) = 0,$	$\theta_f(Y_2) = \theta_s(Y_2) = \theta_{w2},$
$\theta_s''(-Y_1) = 0,$	$\theta_s''(Y_2) = 0,$
$\theta_f''(-Y_1) = -\dfrac{1}{k}[B_1\cosh(2SY_1) - B_2\sinh(2SY_1) + B_3\cosh(SY_1) - B_4\sinh(SY_1) + B_5],$	
$\theta_f''(Y_2) = -\dfrac{1}{k}[B_1\cosh(2SY_2) + B_2\sinh(2SY_2) + B_3\cosh(SY_2) + B_4\sinh(SY_2) + B_5],$	
$\theta_1(-Y_1) = 0,$	$k_{e1}\theta_1'(-1) = Q_{w1},$
$\theta_2(Y_2) = \theta_{w2},$	$k_{e2}\theta_2'(1) = -Q_{w2}.$

In this table, Q_{w1} and Q_{w2} represent the dimensionless heat flux ratios at the outer edges of Wall 1 and Wall 2, respectively. Applying the boundary conditions given by Table 2 allows the analytical solutions of the system of Eqs. (18a), (18d), (19a), and (19b) to be found. The resulting closed-form dimensionless temperature formulations in the radial direction are:

Dimensionless temperature at Wall 2;

$$\theta_2(Y) = C_1 + C_2Y. \qquad\qquad\qquad Y_2 < Y \leq 1 \quad (20a)$$

Dimensionless porous solid phase temperature:

$$\theta_s(Y) = C_3\cosh(2SY) + C_4\cosh(SY) + C_5\cosh(\alpha Y) + C_6\sinh(2SY) \qquad -Y_1 \leq Y < Y_2 \quad (20b)$$
$$+ C_7\sinh(SY) + C_8\sinh(\alpha Y) + C_9Y^2 + C_{10}Y + C_{11}.$$

Dimensionless porous fluid phase temperature:

$$\theta_f(Y) = C_{12}\cosh(2SY) + C_{13}\cosh(SY) + C_{14}\cosh(\alpha Y) + C_{15}\sinh(2SY) \qquad -Y_1 \le Y < Y_2 \qquad (20\text{c})$$
$$+ C_{16}\sinh(SY) + C_{17}\sinh(\alpha Y) + C_{18}Y^2 + C_{19}Y + C_{20},$$

and dimensionless temperature at Wall 1

$$\theta_1(Y) = C_{21} + C_{22}Y. \qquad\qquad\qquad -1 \le Y < -Y_1 \qquad (20\text{d})$$

Substitution of Eqs. (17) and (20a-d) into Eq. (13) reveals the final temperature fields as follows.

Dimensionless temperature field at Wall 1:

$$\theta_1(X,Y) = \frac{X\,[1 + Br'A_4]}{Re\,\Pr k\,(Y_1 + Y_2)\xi} + C_1 + C_2 Y. \qquad\qquad Y_2 < Y \le 1 \qquad (21\text{a})$$

Dimensionless temperature fields in the solid phase of the porous medium:

$$\theta_s(X,Y) = \frac{X\,[1 + Br'A_4]}{Re\,\Pr k\,(Y_1 + Y_2)\xi} + C_3\cosh(2SY) + C_4\cosh(SY) + C_5\cosh(\alpha Y) \qquad -Y_1 \le Y < Y_2 \qquad (21\text{b})$$
$$+ C_6\sinh(2SY) + C_7\sinh(SY) + C_8\sinh(\alpha Y) + C_9 Y^2 + C_{10}Y$$
$$+ C_{11}.$$

Dimensionless temperature field in the fluid phase of the porous medium:

$$\theta_f(X,Y) = \frac{X\,[1 + Br'A_4]}{Re\,\Pr k\,(Y_1 + Y_2)\xi} + C_{12}\cosh(2SY) + C_{13}\cosh(SY) + C_{14}\cosh(\alpha Y) \qquad -Y_1 \le Y < Y_2 \qquad (21\text{c})$$
$$+ C_{15}\sinh(2SY) + C_{16}\sinh(SY) + C_{17}\sinh(\alpha Y) + C_{18}Y^2$$
$$+ C_{19}Y + C_{20},$$

and the dimensionless temperature field at Wall 2:

$$\theta_2(X,Y) = \frac{X\,[1 + Br'A_4]}{Re\,\Pr k\,(Y_1 + Y_2)\xi} + C_{21} + C_{22}Y. \qquad\qquad -1 \le Y < Y_1 \qquad (21\text{d})$$

Next, the governing equation for mass transfer, Eq. (3), is non-dimensionalised and analytically solved using the boundary conditions given in Eq. (4). Considering a control volume over a section of the microchannel and applying a mass balance to this leads to the following equation,

$$\bar{u}\frac{\partial C}{\partial x} = \frac{2k_R}{(h_1 + h_2)}. \qquad\qquad\qquad (22)$$

Assigning C_0 as the initial concentration upon the lower wall at the entrance of the microchannel as an arbitrary initial starting point in the axial direction, the solution of Eq. (22) is

$$C(x) = C_0 \frac{2k_R x}{(h_1 + h_2)\bar{u}}. \qquad\qquad\qquad (23)$$

Thus, the concentration profile in the axial direction is independent of the profile in the transverse direction and the form of solution for the mass transfer profile is similar to that of the temperature profile:

$$C(x,y) = g(y) + h(x). \qquad\qquad\qquad (24)$$

Using the dimensionless parameters defined in Table 1, Eq. (23) can be rendered dimensionless to give the following:

$$\Phi(X) = \frac{2\gamma X}{\xi(Y_1 + Y_2)Pe}, \qquad\qquad\qquad (25)$$

where Φ is the dimensionless concentration; γ is the Damköhler number, relating the reaction rate to the diffusion rate and Pe is the Peclet number, relating the advective to diffusive transport rates.

11

Substitution of Eq. (22) into Eq. (3) gives

$$\frac{2k_R u}{(h_1 + h_2)\bar{u}} = D\frac{\partial^2 C}{\partial y^2} - D_T\frac{\partial^2 T_f}{\partial y^2}. \tag{26}$$

Eq. (26) can now be non-dimensionalised and rearranged into a form that may be readily solved as detailed below,

$$\Phi''(Y) = \frac{2\gamma A_3(A_1\cosh(SY) + A_2\sinh(SY) + Da)}{(Y_1 + Y_2)^2} + \frac{Sr\,k}{\varepsilon(Y_1 + Y_2)}\theta_f''(Y). \tag{27}$$

Since $\theta_f''(Y)$ may be determined from Eq. (20c) only the boundary conditions (4a) and (4b) require expressing in dimensionless form. The results are as follows;

$$\Phi(-Y_1) = 1 \tag{28a}$$

$$\Phi'\left(\frac{Y_2 - Y_1}{2}\right) = \frac{Sr\,k}{\varepsilon(Y_1 + Y_2)}\theta'^{\left(\frac{Y_2-Y_1}{2}\right)}, \tag{28b}$$

in which Sr is the Soret number as defined in Table 1.

Utilisation of the boundary conditions defined by Eqs. (28a) and (28b) facilitate finding the particular solution to Eq. (27) analytically. This results in

$$\Phi(Y) = D_1\cosh(2SY) + D_2\cosh(SY) + D_3\cosh(\alpha Y) + D_4\sinh(2SY) + D_5\sinh(SY) + \tag{29}$$
$$D_6\sinh(\alpha Y) + D_7 Y^2 + D_8 Y + D_9.$$

Finally, substituting Eqs. (25) and (29) into Eq. (24) gives the dimensionless concentration profiles in the axial and transverse directions,

$$\Phi(X,Y) = \frac{2\gamma X}{\xi(Y_1 + Y_2)Pe} + D_1\cosh(2SY) + D_2\cosh(SY) + D_3\cosh(\alpha Y) + D_4\sinh(2SY) \tag{30}$$
$$+ D_5\sinh(SY) + D_6\sinh(\alpha Y) + D_7 Y^2 + D_8 Y + D_9.$$

3.1. Nusselt number

The Nusselt number provides a ratio of the convective to conductive heat transfer taking place across the interface between the walls and the porous fluid phase [57]. The heat transfer coefficients at the bottom and top walls of the microchannel are defined as [57]

$$H_1 = \frac{q_1''}{T_1 - \bar{T}_f}, \tag{31a}$$

$$H_2 = \frac{q_2''}{T_2 - \bar{T}_f}. \tag{31b}$$

Thus, Nusselt number utilising the microchannel height $(h_1 + h_2)$ as the characteristic height, Eqs (31a) and (31b) defining the heat transfer coefficients and k_{ef} as the effective thermal conductivity of the fluid phase may be expressed [57] and converted to the dimensionless terms as follows.

$$Nu_1 = \frac{H_1(h_1 + h_2)}{k_{ef}} = \frac{(Q - 1)(Y_1 + Y_2)}{k\overline{\theta_f}}, \tag{32a}$$

$$Nu_2 = \frac{H_2(h_1 + h_2)}{k_{ef}} = \frac{Q(Y_1 + Y_2)}{k(\theta_{w2} - \overline{\theta_f})}. \tag{32b}$$

The dimensionless bulk mean temperature of the fluid, $\bar{\theta}_f$ may be found by determining a dimensionless form of Eq. (16) and then integrating across the microchannel. This yields,

$$\overline{\theta_f} = \frac{A_3}{(Y_1 + Y_2)} \int_{-Y_1}^{Y_2} \theta_f [A_1 \cosh(SY) + A_2 \sinh(SY) + Da] \, dY. \tag{33}$$

3.2. Sherwood number

In a manner analogous to Nusselt number, Sherwood number provides a measure of the mass transfer taking place at the surface [57]. It is, again, a ratio of the convective mass transport to the diffusive mass transport. Since the reaction taking place on the catalyst surface is of zeroth order, the reaction rate is not dependent upon the concentration of either reactants or products (provided that enough reactant exists to allow for the reaction to proceed). This permits the mass transfer coefficient, H_m to be calculated according to the relation [57];

$$H_m = \frac{k_R}{C_0 - \overline{C}}. \tag{34}$$

With the mass transfer coefficient H_m thus defined, and using the microchannel height $(h_1 + h_2)$ as the characteristic length scale, the Sherwood number may now be expressed in the following form [57] and converted into dimensionless terms;

$$Sh = \frac{(h_1 + h_2)H_m}{D} = \frac{\gamma}{D(1 - \overline{\Phi})}, \tag{35}$$

where the dimensionless bulk concentration, $\overline{\Phi}$ is found in an analogous manner to that of Eq. (33),

$$\overline{\Phi} = \frac{A_3}{(Y_1 + Y_2)} \int_{-Y_1}^{Y_2} \Phi [A_1 \cosh(SY) + A_2 \sinh(SY) + Da] \, dY. \tag{36}$$

3.3. Entropy generation

In order to examine the entropy generation of the system, contributions from different sources are considered separately and then as a whole, to yield an understanding as to how each component contributes to the whole. Following the literature [18,37,58,59], the system has been split into contributions from Wall1, the solid porous matrix heat transfer, the fluid heat transfer, the fluid friction component and that of the mass transfer. The volumetric entropy generations for the system are expressed by the equations listed below [18,36,38].

The term, $\dot{S}_2'''$ accounts for the entropy generation in the Wall 2, the upper wall

$$\dot{S}_2''' = \frac{k_2}{T_2^2} \left[\left(\frac{\partial T_2}{\partial x} \right)^2 + \left(\frac{\partial T_2}{\partial y} \right)^2 \right], \tag{37a}$$

Entropy generation in the solid phase of the porous medium due to heat transfer may be calculated using $\dot{S}_S'''$.

$$\dot{S}_S''' = \frac{k_{es}}{T_S^2} \left[\left(\frac{\partial T_S}{\partial x} \right)^2 + \left(\frac{\partial T_S}{\partial y} \right)^2 \right] - \frac{h_{sf} a_{sf} (T_S - T_f)}{T_S}, \tag{37b}$$

Similarly, $\dot{S}_f'''$ is used to find the entropy generation rate in the fluid phase.

$$\dot{S}_f''' = \frac{k_{ef}}{T_f^2} \left[\left(\frac{\partial T_f}{\partial x} \right)^2 + \left(\frac{\partial T_f}{\partial y} \right)^2 \right] + \frac{h_{sf} a_{sf} (T_S - T_f)}{T_f}. \tag{37c}$$

Fluid friction irreversibility is accounted for by $\dot{S}_{FF}'''$.

$$\dot{S}_{FF}''' = \frac{\mu_f}{\kappa \, T_f} u^2 + \frac{\mu_{eff}}{T_f} \left(\frac{du}{dy} \right)^2. \tag{37d}$$

Irreversibility sources due to the combination of concentration gradients and also those due to mixed thermal and concentration gradients are found using the equation for $\dot{S}_{DI}'''$.

13

$$\dot{S}_{DI}''' = \frac{R\,D}{C}\left[\left(\frac{\partial C}{\partial x}\right)^2 + \left(\frac{\partial C}{\partial y}\right)^2\right] + \frac{R\,D}{T_f}\left[\left(\frac{\partial C}{\partial x}\right)\left(\frac{\partial T_f}{\partial x}\right) + \left(\frac{\partial C}{\partial y}\right)\left(\frac{\partial T_f}{\partial y}\right)\right].$$ (37e)

Finally, the irreversibility in the lower wall, Wall 1 is defined as

$$\dot{S}_1''' = \frac{k_1}{T_1^2}\left[\left(\frac{\partial T_1}{\partial x}\right)^2 + \left(\frac{\partial T_1}{\partial y}\right)^2\right].$$ (37f)

To non-dimensionalise Eqs. (37a-f) the following parameters are required. These are the dimensionless entropy generation, dimensionless heat flux and an irreversibility distribution ratio, respectively.

$$N_i = \frac{\dot{S}_i''' h_3^2}{k_{es}} \qquad i = 1, s, f, FF, DI, 2$$ (38)

$$\omega = \frac{(q_1'' + q_2'')h_3}{2k_{es}T_{w,in}},$$ (39)

$$\varphi = \frac{RDC_0}{k_{es}}.$$ (40)

The resultant dimensionless versions of Eqs. (37a-f) are:

Dimensionless entropy generation in the Wall 2, or the upper wall;

$$N_2 = \frac{k_{e2}\omega^2}{(\omega\theta_2 + 1)^2}\left[\xi^2\left(\frac{\partial\theta_2}{\partial X}\right)^2 + \left(\frac{\partial\theta_2}{\partial Y}\right)^2\right]. \qquad Y_2 \le Y < 1 \quad (41a)$$

Dimensionless entropy generation in the solid phase of the porous medium due to heat transfer

$$N_s = \frac{\omega^2}{(\omega\theta_s + 1)^2}\left[\xi^2\left(\frac{\partial\theta_s}{\partial X}\right)^2 + \left(\frac{\partial\theta_s}{\partial Y}\right)^2\right] - \frac{Bi\omega(\theta_s - \theta_f)}{(\omega\theta_s + 1)}. \qquad -Y_1 \le Y < Y_2 \quad (41b)$$

Similarly, the dimensionless entropy generation rate in the fluid phase is expressed by

$$N_f = \frac{k\,\omega^2}{(\omega\theta_f + 1)^2}\left[\xi^2\left(\frac{\partial\theta_f}{\partial X}\right)^2 + \left(\frac{\partial\theta_f}{\partial Y}\right)^2\right] + \frac{Bi\omega(\theta_s - \theta_f)}{(\omega\theta_f + 1)}. \qquad -Y_1 \le Y < Y_2 \quad (41c)$$

Dimensionless fluid friction irreversibility is accounted for by

$$N_{FF} = \frac{A_6\omega}{(\theta_f\omega + 1)}[Da^2 + 2A_1Da\cosh(SY) + 2A_2Da\sinh(SY) \qquad -Y_1 \le Y < Y_2 \quad (41d)$$
$$+ (A_1^2 + A_2^2)\cosh(2SY) + 2A_1A_2\sinh(2SY)].$$

Dimensionless irreversibility sources due to the combination of concentration gradients and those due to mixed thermal and concentration gradients are found using;

$$N_{DI} = \frac{\varphi}{\Phi}\left[\xi^2\left(\frac{\partial\Phi}{\partial X}\right)^2 + \left(\frac{\partial\Phi}{\partial Y}\right)^2\right] + \frac{\varphi\omega}{(\omega\theta_f + 1)}\left[\xi^2\left(\frac{\partial\Phi}{\partial X}\right)\left(\frac{\partial\theta_f}{\partial X}\right) + \left(\frac{\partial\Phi}{\partial Y}\right)\left(\frac{\partial\theta_f}{\partial Y}\right)\right]. \qquad -Y_1 \le Y < Y_2 \quad (41e)$$

At the lower wall, Wall 1, the dimensionless entropy generation rate is;

$$N_1 = \frac{k_{e1}\omega^2}{(\omega\theta_1 + 1)^2}\left[\xi^2\left(\frac{\partial\theta_1}{\partial X}\right)^2 + \left(\frac{\partial\theta_1}{\partial Y}\right)^2\right]. \qquad -1 \le Y < -Y_1 \quad (41f)$$

To facilitate the study of entropy generation and compare the contributions from different sources of irreversibility, the equations for the fluid and the solid phases of the porous medium are broken down. This provides the following equations for the irreversibility of heat transfer in the system.

$$N_{s,ht} = \frac{\omega^2}{(\omega\theta_s + 1)^2}\left[\xi^2\left(\frac{\partial\theta_s}{\partial X}\right)^2 + \left(\frac{\partial\theta_s}{\partial Y}\right)^2\right],$$ (42a)

$$N_{f,ht} = \frac{k\,\omega^2}{(\omega\theta_f + 1)^2}\left[\xi^2\left(\frac{\partial\theta_f}{\partial X}\right)^2 + \left(\frac{\partial\theta_f}{\partial Y}\right)^2\right]. \tag{42b}$$

By adding the components of Eqs. (41b) and (41c) the interstitial volumetric entropy generation term can be expressed by,

$$N_{int} = \frac{Bi\,\omega^2(\theta_f - \theta_s)^2}{(\omega\theta_s + 1)(\omega\theta_f + 1)}. \tag{43}$$

The volumetric entropy generations for the porous insert as a whole, N_{pm} is the sum of the equations that describe the various irreversibility sources with the porous medium only. Thus, N_{pm} contains terms for the combined processes of heat transfer, viscous dissipation, and concentration gradients,

$$N_{pm} = N_{s,ht} + N_{f,ht} + N_{int} + N_{FF} + N_{DI}. \tag{44}$$

For the total entropy generation in the microreactor, N_{Tot}, the sum of the parts of volumetric entropy generation, in the ranges in which they are valid, is integrated over the volume of the microchannel with the inclusion of contributions from the walls. That is

$$N_{Tot} = \int_{-1}^{1}\int_{0}^{1}\sum N_i\,dXdY, \qquad i = 1, s, f, FF, DI, 2. \tag{45}$$

3.4. Validation

Appendix B1 shows that the analytical solution of the temperature fields developed in Section 3 can be rigorously reduced to those of Ting et al. [38] and Hunt et al. [17] for a two-dimensional porous microchannel. This is achieved by ignoring the catalytic surfaces and changing the heat flux at the outer surface such that the configuration shown in Fig. 1 is converted to that in Ref. [17] in the absence of surface heat generation (i.e. Ref [38]). The temperature field and the average Nusselt number obtained from the current analytical solution in the limit of very large porosity (and permeability) are further compared to those computed through solving Navier-Stokes and energy equations in a clear microchannel with thick walls and exothermic internal surfaces. The details of this comparison, which confirms the validity of Eqs. (6b) and (6c) and the subsequent analytical solutions, are given in Appendix B2.

4. Results and discussions
4.1. Temperature fields

The default parametric values are presented in Table 3 and include an asymmetric thermal loading on the upper and lower internal walls of the microreactor. Figures 2-4 show contour plots of the dimensionless temperature field in the microreactor including the upper and lower walls. It is important to note that the non-dimensionalisation described by Table 1 allows some parts of the system to have negative non-dimensional temperatures. Figures 2-4 show the temperature fields of the fluid and solid phases, while all subfigures include the temperature field of the solid walls. A general feature of these figures is the clear distinction between the temperature fields of the fluid and porous solid phases, rendering a strong deviation from local thermal equilibrium (LTE). This is consistent with the findings of the previous investigations of internally heat generating porous channels [25,48,60] and highlights the significance of LTNE approach in the current analysis. The effects of variation in the thermal conductivity ratio, k, are shown in Fig. 2. A decrease in k can be accomplished by increasing the thermal conductivity of the porous solid, decreasing that of the fluid or a combination of both. The

net effect is more heat transmitted to the centre of the microchannel by the solid and less conducted or convected away by the fluid. Figure 2 illustrates this point, showing a progressively widen temperature range for decreasing k. This result is of practical significance, demonstrating that the respective thermal conductivities of the fluid and porous solid can have a major impact on the temperatures encountered in the microreactor.

Increasing Reynolds number (defined in Table 1) represents an increase in the velocity field of the fluid in the microreactor. Figure 3 shows the effects of flow velocity upon the dimensionless temperature field of the microreactor. At lower Reynolds numbers, the implied lower velocity allows for longer residence times of the fluid element and hence greater quantities of thermal energy is imparted to the fluid. Further, quite expectedly, the rate of heat removal from the system by convection is lower at reduced flow velocities. The combination of these effects leads to a significantly larger axial temperature gradient and higher dimensionless temperatures at lower Reynolds numbers. Once again, from a practical point of view, control of the fluid velocity within the microreactor allows for variation in the temperature fields.

Consistent with the one-dimensional analyses in microreactors [18,19,36], and also with those in both axial and transverse directions [17], Fig. 4 shows that increasing the thickness of the upper wall extends the range of dimensionless temperatures. The corresponding decrease in microchannel thickness gives rise to an increase in velocity field of the microchannel and a decrease in the volume of fluid. Thus the same total heat flux is applied to a smaller volume of porous medium, which is hence less able to convect heat away, leading to higher temperatures. The greater disparity between the temperatures of the two phases towards the centreline is indicative of a deviation from local thermal equilibrium, which clearly reflects the necessity of taking an LTNE approach in the current problem. This, in turn, highlights the importance of the extended interface model developed in Section 3.

4.2. Nusselt number

Variation of Nusselt number on the wall versus the upper wall thickness is shown in Figs. 5c and 5d as calculated on the lower and upper walls, respectively. Similar examination for the Nusselt number against the lower wall thickness is shown in Figs. 5a and 5b. In all cases, the general trend is towards a significant increase in Nusselt number as the wall thickness decreases. This is in keeping with the findings of the recent works [17,18] and reinforces the emerging notion that the enclosing structure plays a vital role in determining the thermal characteristics of the microreactor. Decreasing the thermal conductivity ratio causes a monotonically increasing Nusselt number on the upper wall under the given conditions. This behaviour is consistent with that observed in Fig. 4 in which decreasing the thermal conductivity ratio widens the temperature range encounter in the microreactor. However, as the wall thickness increases the Nusselt number on the lower wall behaves in a more complex manner. For thick walled systems, the behaviour of the system changes with higher thermal conductivity ratios. This can be seen in Figs. 5a and 5c, where the curves for $k = 0.2$ and $k = 0.5$ reach first an intersection, then cross over one another. This behaviour indicates the presence of minima in the variation of Nusselt number against thermal conductivity ratio for a given wall thickness above the threshold value. Clearly, existence of such minima enables thermal optimisation of the system.

Changes in Nusselt number due to variations in the wall thickness are examined in Fig. 6. Utilising the findings of Fig. 5, a value of k was set to 0.5 in Fig. 6. While maintaining the magnitude of the total thermal load constant, the individual fluxes from the catalyst into the porous microchannel are varied through a measure of

their proportionality, Q defined in Table 1. Figure 6 shows a monotonic increase in Nusselt number, for all cases, as the wall thickness decreases. This holds regardless of whether there is an imbalance of heat flux from the upper or the lower wall or if the Nusselt number is measured on the upper (Figs. 6b and 6d) or lower wall (Figs. 6a and 6c). Nonetheless, variations in Q appear to have considerable influences upon the numerical value of Nusselt number. Importantly, a feature of all graphs is the point of intersection at which the lines cross regardless of the thermal load balance. Further values of Q were tested for completeness, these demonstrated that the point of intersection holds for all values of Q. This indicates the existence of a critical value of the wall thickness for which the Nusselt number becomes independent of the magnitude of the dimensionless surface heat flux ratio (Q).

4.3. Concentration fields

The dimensionless concentration contours along the full length of the microchannel are shown in Figs. 7a and 8a. Due to the high aspect ratio of the microchannel, a more representative visualisation of the concentration contours can be achieved by examining a segment of the microchannel (parts b, c, and d of Figs. 7 and 8). These figures show the advection of species along the length of the microchannel in the flow direction and the axial increase in the concentration due to reaction on the catalyst surfaces. Parts b, c, and d of Fig. 7 show the effect of increasing Damköhler number on the concentration field. Clearly, there is an increase in the magnitude and range of the concentration contours, which is indicative of an increase of concentration in the axial direction. This is an anticipated consequence of increasing Damköhler number, since it is directly related to the reaction rate on the catalyst surface. Close examination further reveals an increase in the magnitude and range of the concentration in the transverse direction. It is likely that this is also a result of the enhanced production of species on the catalytic surface coupled with the velocity of the flow causing a greater differential between the centre of the porous microchannel and the channel walls.

Investigating the effect of thickening of either the upper or lower wall demonstrates the strong influences of the wall thickness upon the concentration field. Figures 8b to 8d show that increasing thickness of the upper wall can cause a significant increase in the magnitude of the concentration in the microchannel. The associated decrease in volume coupled with the same surface area of catalyst contributes to the observed higher concentration. Additionally, the increased temperatures under these conditions (Fig. 4) augment mass transfer due to the Soret effect. This is an important point to note from microreactor design viewpoint. In the use of microreactors for chemical synthesis, the drive towards increased yield is a key consideration. Thus, the methods by which the magnitude of the species concentration can be increased are desirable.

4.4. Sherwood number

The response of Sherwood number to variation in the microchannel thickness is shown in Fig. 9a. Here it can be seen that as the microchannel height increases with respect to the wall thickness, there is a corresponding increase in Sherwood number. Increase of heat transfer at thinner walls strengthens the thermal diffusion of mass and enhances the mass transfer process. The graph is nearly a straight line and indicates a linear relationship. It is important to observe the fact that the Sherwood number is constant for a given microchannel thickness. This is best demonstrated by examining the Sherwood number for $Y_1 = 0.5$ and the line for $Y_2 = 0.8$ (which leads to a dimensionless microchannel thickness of 1.3) and comparing with the Sherwood number for $Y_1 = 0.9$ and the line for $Y_2 = 0.4$ (which also has a dimensional microchannel thickness of 1.3). Clearly, these both have an equal

Sherwood number. Evidenced by this is that the symmetry or lack thereof for any set of wall thicknesses is not as important as the microchannel thickness.

Thermal conductivity ratio, k, also causes a linear increase of Sherwood number with the lower wall thickness, Y_1 as shown in Fig. 9b. However, the increase in the value of thermal conductivity ratio renders a non-linear behaviour, as shown in Fig. 9d. This is related to the feature observed in Fig. 5, where Nusselt number was found to be much higher at low values of k. Higher rates of heat transfer enhances the Soret effect and magnifies the value of Sherwood number. Further, variation in Biot number (Fig. 9c) generally has little effects upon the Sherwood number, except at very low Biot number, where the flow of thermal energy between the solid and fluid phases of the porous medium is largely inhibited. The observed reduction of Sherwood number at low Biot number demonstrates that consideration should be given to LTNE effects in thermochemical, porous microreactors. It should be clarified that although the qualitative trends discussed here remain almost unchanged, altering the value of Soret number widens the range of changes in Sherwood number.

4.5. Local and total entropy generation

Figures 10 and 11 represent an investigation of the local entropy generation. They contain 6 contour plots pertaining to the various terms of Eq. (41) and (42), enabling examination of the effects of changing one parameter on separate aspects of the microchannel. Since the entropy generation contribution from the solid walls is only dependent upon temperature within that particular wall, the entropy generation within the walls is not that enlightening and is therefore omitted. Both Figs. 10a and 10b show asymmetry consistent with the heat flux ratio of the system in which there is a greater heat flux at the upper wall than at the lower wall. The contours of the entropy generation due to interstitial heat transfer suggest a greater generation of entropy from this source at the centre of the microchannel. This is entirely consistent with Figs. 2 to 5 where the temperature difference between the solid and fluid phases of the porous medium are larger towards the centre of the microchannel and decrease towards the walls. Entropy generation due to hydrodynamic effects, Fig. 10d, shows that maximum values are encountered at the interface between the fluid and the walls due to the dominance of viscous effects in this vicinity. The irreversibility then decreases rapidly moving away from the wall before building to a moderate level in the centre of the microchannel where the velocity is maximum and thus increases the irreversibility. Entropy generation due to mass transfer is shown in Fig. 10e, and as expected, the greater levels of irreversibility are to be found on the walls next to the catalytic surfaces. It is worthy of note that the magnitude of the mass transfer contribution is significantly greater than that of other sources. This leads to Fig. 10f, which shows the combined local entropy generation by the porous insert is dominated by the mass transfer contribution. However, the dominance of mass transfer irreversibility can be overcome by increasing the heat flux or reducing Damköhler number [17].

As shown in Fig. 11, setting the wall thicknesses to be increasingly asymmetric increases the magnitude of the sources of irreversibility. The least affected by this is the solid phase of the porous medium. Other contributions show increases in magnitude of over 50%. The entropy generation due to fluid friction shows an increase in the thickness of the highly irreversible zone along the centreline of the porous insert. Narrowing of the microchannel thickness leading to enhanced velocities at the centre of the insert are the root cause of this effect. An increase in magnitude of the mass transfer irreversibility contribution is to be expected. This can be confirmed

by examination of Figs. 4 and 8, which show the effects of increasing the asymmetry of the thick walls upon the temperature and concentration fields, respectively.

Calculation of the total entropy generation of the system includes adding all the sources examined above as well as those of the upper and lower walls as defined by Eq. (41). Varying the thermal conductivity ratio appears to have a strong influence upon the total entropy of the system. From Fig. 12a, it is readily observed that this progression is non-linear in nature and has a more pronounced effect at lower thermal conductivity ratios. As already discussed, low values of thermal conductivity ratio can significantly enhance the rates of heat transfer and thus smoothen the temperature gradients in the system, which reduces the thermal irreversibility of the system. Magnifying the value of Soret number on this graph also result in an increase in the total entropy generation, the magnitude of this increase is most pronounced for higher values of thermal conductivity ratio. The low value of thermal conductivity ratio used as the default value for the previous sections of this study show very small differences. Thus, an increased base value for the thermal conductivity was chosen for the purposes of clarity (see Table 3).

Figure 12b depicts the total rate of entropy generation against Damköhler number for several values of Soret number, illustrating the strong influence of Damköhler number upon the total irreversibility of the system. Higher rates of catalytic reaction at enhanced values of Damköhler number intensify the mass transfer rate and thus magnify the associated irreversibility. Figure 12b shows that for a given Damköhler number increasing the value of Soret number leads to an increase in the total entropy generation. Nonetheless, regardless of the value of Soret number the total irreversibility always increases monotonically against Damköhler number. Figures 12c and 12d show variations of the total entropy generation with the dimensionless heat flux, ω. Clearly, increasing the exothermicity of the catalytic reaction, implied by the higher values of ω, strongly intensifies the total rate of entropy generation due to strengthening of the thermal irreversibilities. Increasing the value of Damköhler number (Fig. 12c) and narrowing the microchannel (Fig. 12d) further increase the total irreversibility by promoting the mass transfer and thermal irreversibilities, respectively.

5. Conclusions

A two-dimensional, analytical local thermal non-equilibrium model of transport of heat and mass was developed for an asymmetric microreactor, accommodating an exothermic catalytic reaction. The thermal diffusion of mass was taken into account and thus mass transfer was coupled to the thermal fields. The catalyst was placed on the internal surface of the walls and therefore heat of reaction was released on a surface in contact with the solid wall, fluid phase and porous solid phase. Such configuration is distinctively different to that of volumetric heat release investigated in the earlier studies, as it provides three different routes for heat diffusion, whilst currently there is no model to describe the heat transfer split amongst these. The issue was resolved by extending an existing model of porous interfaces (Model A of Vafai and co-workers [44]). The validity of the extended model was demonstrated by comparing the analytically calculated temperature fields and Nusselt number with those predicted computationally in the limit of very large porosity and permeability. Further, it was shown that the analytical solution could be systematically reduced to the theoretical formulations on simpler configurations. The extended interface model can be used in future theoretical and numerical studies of microreactors. Further, the developed close-form analytical solutions can serve as a means of validation for the

relevant theoretical analyses. Most importantly, the study revealed some key physical points as summarised below.

- It was shown that asymmetry in heat transfer in the upper and lower parts of the system, arising from the thermal and structural asymmetry of the microreactor, had a pronounced effect upon the temperature and concentration fields and that the system can significantly deviates from the local thermal equilibrium.

- Of the large number of parameters examined in the study, wall thickness was shown to be highly influential in the Nusselt number, thermal and concentration fields. Thus, demonstrating the importance of its inclusion in microreactor models.

- Thickness of the enclosing walls has a much greater impact on the Sherwood number than asymmetry of the enclosing structure.

- The thermal conductivity ratio also has a strong effect upon the Nusselt number, temperature fields and rate of heat transfer.

- The Nusselt number was found to have a singular point for a given wall thickness where any change in heat flux ratio would yield the same Nusselt number. This effect was found to exist on both the upper and lower walls. The singular point could be exploited to allow for greater thermal control of a microreactor.

- Exothermicity of the reaction was found to promote the total irreversibility of the system in a monotonic manner. Further, increasing Damköhler number appeared to have a strong intensifying effect on the total generation of entropy, while the effects of Soret number were less pronounced.

Acknowledgment

Appendix A: Closed-form constants

Provided here is a list of the closed form constants.

$$A_1 = \frac{Da[\sinh(SY_1) + \sinh(SY_2)]}{\cosh(SY_2)\sinh(SY_1) + \cosh(SY_1)\sinh(SY_2)}, \tag{A1a}$$

$$A_2 = \frac{Da[\cosh(SY_2) - \cosh(SY_1)]}{\cosh(SY_2)\sinh(SY_1) + \cosh(SY_1)\sinh(SY_2)}, \tag{A1b}$$

$$A_3 = \frac{S(Y_1 + Y_2)}{DaS(Y_1 + Y_2) + A_1(\sinh(SY_1) + \sinh(SY_2)) + A_2(\cosh(SY_2) - \cosh(SY_1))}, \tag{A1c}$$

$$\begin{aligned} A_4 = \frac{SA_3}{2}[&2Da^2S(Y_1 + Y_2) + 4A_2Da(\cosh(SY_2) - \cosh(SY_1)) \\ &+ 2A_1A_2(\cosh(2SY_2) - \cosh(2SY_1)) + 4A_1Da(\sinh(SY_1) + \sinh(SY_2)) \\ &+ (A_1^2 + A_2^2)(\sinh(2SY_1) + \sinh(2SY_2))], \end{aligned} \tag{A1d}$$

$$A_5 = \frac{A_3(1 + Br'A_4)}{(Y_1 + Y_2)}, \tag{A1e}$$

$$A_6 = A_3^2 Br'^{S^2}, \tag{A1f}$$

$$B_1 = (A_1^2 + A_2^2)A_6, \qquad\qquad B_2 = 2A_1A_2A_6, \qquad\qquad \text{(A2a,b)}$$

$$B_3 = (2A_1A_6Da - A_1A_5), \qquad\qquad B_4 = (2A_2A_6Da - A_2A_5), \qquad\qquad \text{(A2c,d)}$$

$$B_5 = Da(A_6Da - A_5), \qquad\qquad \text{(A2e)}$$

$$C_1 = \frac{Q_{w2}2Y_2}{k_{e2}} + \theta_{w2}, \qquad\qquad C_2 = \frac{Q_{w2}}{k_{e2}}, \qquad\qquad \text{(A3a,b)}$$

$$C_3 = \frac{B_1Bi}{16kS^4 - 4kS^2\alpha^2}, \qquad\qquad C_4 = \frac{B_3Bi}{kS^4 - kS^2\alpha^2}, \qquad\qquad \text{(A3c,d)}$$

$$\text{(A3e)}$$
$$\begin{aligned}
C_5 = \frac{1}{k\alpha^4(4S^4 - 5S^2\alpha^2 + \alpha^4)}\, & Bi\ \text{csch}((Y_1 + Y_2)\alpha)\big[\big(B_5(4S^4 - 5S^2\alpha^2 + \alpha^4) \\
& + \alpha^2(B_3(-4S^2 + \alpha^2)\cosh(2SY_2) + B_1(-S^2 + \alpha^2)\cosh(2SY_2) \\
& + B_4(-4S^2 + \alpha^2)\sinh(2SY_2) + B_2(-S + \alpha)(S + \alpha)\sinh(2SY_2))\big)\sinh(\alpha Y_1) \\
& + (B_3\alpha^2(-4S^2 + \alpha^2)\cosh(SY_1) + B_1\alpha^2(-S + \alpha)(S + \alpha)\cosh(2SY_1) \\
& + (4S^2 - \alpha^2)(B_5(S - \alpha)(S + \alpha) + B_4\alpha^2\sinh(SY_1)) \\
& + B_2(S - \alpha)\alpha^2(S + \alpha)\sinh(2SY_1))\sinh(\alpha Y_2)\big],
\end{aligned}$$

$$C_6 = \frac{B_2Bi}{16kS^4 - 4kS^2\alpha^2}, \qquad\qquad C_7 = \frac{B_4Bi}{kS^4 - kS^2\alpha^2}, \qquad\qquad \text{(A3f,g)}$$

$$\text{(A3h)}$$
$$\begin{aligned}
C_8 = \frac{1}{k\alpha^4(4S^4 - 5S^2\alpha^2 + \alpha^4)} & Bi\ \text{csch}((Y_1 + Y_2)\alpha)\big[\cosh(\alpha Y_2)\big(-B_5(4S^4 - 5S^2\alpha^2 + \alpha^4) \\
& + \alpha^2(B_3(4S^2 - \alpha^2)\cosh(SY_1) + B_1(S - \alpha)(S + \alpha)\cosh(2SY_1) \\
& + B_4(-4S^2 + \alpha^2)\sinh(SY_1) + B_2(-S^2 + \alpha^2)\sinh(2SY_1))\big) \\
& + \cosh(\alpha Y_1)\big(B_5(4S^4 - 5S^2\alpha^2 + \alpha^4) \\
& + \alpha^2(B_3(-4S^2 + \alpha^2)\cosh(SY_2) + B_1(-S^2 + \alpha^2)\cosh(2SY_2) \\
& + B_4(-4S^2 + \alpha^2)\sinh(SY_2) + B_2(-S + \alpha)(S + \alpha)\sinh(2SY_2))\big)\big],
\end{aligned}$$

$$C_9 = -\frac{B_5Bi}{2k\alpha^2}, \qquad\qquad \text{(A3i)}$$

$$\text{(A3j)}$$
$$\begin{aligned}
C_{10} = \frac{1}{4kS^2(Y_1 + Y_2)\alpha^2}\Big(& 2S^2\big(B_5Bi(-Y_1^2 + Y_2^2) + 2k\alpha^2\theta_{w2}\big) \\
& + Bi\big(-4B_3\cosh(SY_1) - B_1\cosh(2SY_1) + 4B_3\cosh(SY_2) + B_1\cosh(2SY_2) \\
& + 4B_4(\sinh(SY_1) + \sinh(SY_2)) + B_2(\sinh(2SY_1) + \sinh(2SY_2))\big)\Big),
\end{aligned}$$

$$\text{(A3k)}$$
$$\begin{aligned}
C_{11} = \frac{1}{4kS^2(Y_1 + Y_2)\alpha^4}\Big(& 2S^2\big(B_5Bi(Y_1 + Y_2)(-2 + Y_1Y_2\alpha^2) + 2kY_1\alpha^4\theta_{w2}\big) \\
& + Bi\alpha^2\big(4B_3Y_2\cosh(SY_1) + B_1Y_2\cosh(2SY_1) \\
& - 2Y_2(2B_4 + B_2\cosh(SY_1))\sinh(SY_1) \\
& + Y_1(4B_3\cosh(SY_2) + B_1\cosh(2SY_2) + 4B_4\sinh(SY_2) + B_2\sinh(2SY_2))\big)\Big),
\end{aligned}$$

$$C_{12} = \frac{B_1(Bi - 4S^2)}{4kS^2(4S^2 - \alpha^2)}, \qquad\qquad C_{13} = -\frac{B_3(-Bi + S^2)}{kS^2(S^2 - \alpha^2)}, \qquad\qquad \text{(A3l,m)}$$

$$\text{(A3n)}$$
$$\begin{aligned}
C_{14} = \frac{1}{k\alpha^4(4S^4 - 5S^2\alpha^2 + \alpha^4)}\big(Bi \\
- \alpha^2\big)\text{csch}((Y_1 + Y_2)\alpha)\Big(& \big((B_5(4S^4 - 5S^2\alpha^2 + \alpha^4) \\
& + \alpha^2(B_3(-4S^2 + \alpha^2)\cosh(SY_2) + B_1(-S^2 + \alpha^2)\cosh(2SY_2) \\
& + B_4(-4S^2 + \alpha^2)\sinh(SY_2) + B_2(-S + \alpha)(S + \alpha)\sinh(2SY_2))\big)\sinh(\alpha Y_1) \\
& + (B_3\alpha^2(-4S^2 + \alpha^2)\cosh(SY_1) + B_1\alpha^2(-S + \alpha)(S + \alpha)\cosh(2SY_1) \\
& + (4S^2 - \alpha^2)(B_5(S - \alpha)(S + \alpha) + B_4\alpha^2\sinh(SY_1)) \\
& + B_2(S - \alpha)\alpha^2(S + \alpha)\sinh(2SY_1))\sinh(\alpha Y_2)\Big),
\end{aligned}$$

$$C_{15} = \frac{B_2(Bi - 4S^2)}{4kS^2(4S^2 - \alpha^2)}, \qquad\qquad C_{16} = -\frac{B_4(-Bi + S^2)}{kS^2(S^2 - \alpha^2)}, \qquad\qquad \text{(A3o,p)}$$

$$\text{(A3q)}$$
$$\begin{aligned}
C_{17} = \frac{1}{k\alpha^4(4S^4 - 5S^2\alpha^2 + \alpha^4)}\, & (Bi - \alpha^2)\text{csch}((Y_1 + Y_2)\alpha)(\cosh(\alpha Y_2) - B_5(4S^4 - 5S^2\alpha^2 + \alpha^4) \\
& + \alpha^2(B_3(4S^2 - \alpha^2)\cosh(SY_1) + B_1(S - \alpha)(S + \alpha)\cosh(2SY_1) + B_4(-4S^2 \\
& + \alpha^2)\sinh(SY_1) + B_2(-S^2 + \alpha^2)\sinh(2SY_1))) + \cosh(\alpha Y_1)(B_5(4S^4 - 5S^2\alpha^2 \\
& + \alpha^4) + \alpha^2(B_3(-4S^2 + \alpha^2)\cosh(SY_2) + B_1(-S^2 + \alpha^2)\cosh(2SY_2) \\
& + B_4(-4S^2 + \alpha^2)\sinh(SY_2) + B_2(-S + \alpha)(S + \alpha)\sinh(2SY_2)))),
\end{aligned}$$

$$C_{18} = -\frac{B_5 \text{Bi}}{2k\alpha^2}, \qquad\qquad\qquad C_{19} = C_{11}, \qquad\qquad\qquad \text{(A3r,s)}$$

$$
\begin{aligned}
C_{20} = \frac{1}{4kS^2(Y_1 + Y_2)\alpha^4}\Big(& 2S^2\big(B_5(Y_1 + Y_2)(-2\text{Bi} + (2 + \text{Bi}Y_1Y_2)\alpha^2) + 2kY_1\alpha^4\theta_{w2}\big) \\
& + \text{Bi}\alpha^2\big(4B_3Y_2\cosh(SY_1) + B_1Y_2\cosh(2SY_1) \\
& - 2Y_2(2B_4 + B_2\cosh(SY_1))\sinh(SY_1) \\
& + Y_1(4B_3\cosh(SY_2) + B_1\cosh(2SY_2) + 4B_4\sinh(SY_2) + B_2\sinh(2SY_2))\big)\Big),
\end{aligned}
$$

(A3t)

$$C_{21} = \frac{Q_{w1}Y_1}{k_{e1}}, \qquad\qquad\qquad C_{22} = \frac{Q_{w1}}{k_{e1}}, \qquad\qquad\qquad \text{(A3u,v)}$$

$$
\begin{aligned}
C_{23} = \frac{1}{4kS^2(Y_1 + Y_2)\alpha^2}\text{Bi}\Big(& -2B_5S^2{Y_1}^2 + 2B_5S^2{Y_2}^2 - 4B_3\cosh(SY_1) - B_1\cosh(2SY_1) \\
& + 4B_3\cosh(SY_2) + B_1\cosh(2SY_2) + 4B_4\sinh(SY_1) + B_2\sinh(2SY_1) \\
& + 4B_4\sinh(SY_2) + B_2\sinh(2SY_2)\Big),
\end{aligned}
$$

(A3w)

$$
\begin{aligned}
\theta_{w2} = ((Y_1 + Y_2)/(1 + k))\Big(& Q \\
& - \big(2C_9Y_2 + 2C_{18}kY_2 + (C_7 + C_{16}k)S\cosh(SY_2) + 2(C_6 + C_{15}k)S\cosh(2SY_2) \\
& + C_8\alpha\cosh(\alpha Y_2) + C_{17}k\alpha\cosh(\alpha Y_2) + C_4S\sinh(SY_2) + C_{13}kS\sinh(SY_2) \\
& + 2C_3S\sinh(2SY_2) + 2C_{12}kS\sinh(2SY_2) + C_5\alpha\sinh(\alpha Y_2) + C_{14}k\alpha\sinh(\alpha Y_2) \\
& + (C_{23} + kC_{23})\big)\Big),
\end{aligned}
$$

(A3x)

$$D_1 = \frac{C_{12}kSr(Y_1 + Y_2)}{(Y_1 + Y_2)^2\varepsilon}, \qquad\qquad D_2 = \frac{(C_{13}kSrS^2(Y_2 + Y_1) + 2A_1A_3\gamma\varepsilon)}{S^2(Y_1 + Y_2)^2\varepsilon}, \qquad \text{(A4a,b)}$$

$$D_3 = \frac{C_{14}kSr(Y_1 + Y_2)}{(Y_1 + Y_2)^2\varepsilon}, \qquad\qquad D_4 = \frac{C_{15}kSr(Y_1 + Y_2)}{(Y_1 + Y_2)^2\varepsilon}, \qquad \text{(A4c,d)}$$

$$D_5 = \frac{(C_{16}kS^2Sr(Y_1 + Y_2) + 2A_2A_3\gamma\varepsilon)}{S^2(Y_1 + Y_2)^2\varepsilon}, \qquad\qquad D_6 = \frac{C_{17}kSr(Y_1 + Y_2)}{(Y_1 + Y_2)^2\varepsilon}, \qquad \text{(A4e,f)}$$

$$D_7 = \frac{(C_{18}kSr(Y_1 + Y_2) + A_3\text{Da}\gamma\varepsilon)}{(Y_1 + Y_2)^2\varepsilon}, \qquad \text{(A4g)}$$

$$
\begin{aligned}
D_8 = \frac{1}{S(Y_1 + Y_2)^2\varepsilon}\Big(& C_{19}kSSrY_1 + C_{19}kSSrY_2 + A_3\text{Da}SY_1\gamma\varepsilon - A_3\text{Da}SY_2\gamma\varepsilon \\
& - 2A_2A_3\gamma\varepsilon\cosh\left(\frac{1}{2}S(-Y_1 + Y_2)\right) - 2A_1A_3\gamma\varepsilon\sinh\left(\frac{1}{2}S(-Y_1 + Y_2)\right)\Big),
\end{aligned}
$$

(A4h)

$$
\begin{aligned}
D_9 = \frac{1}{S^2(Y_1 + Y_2)^2\varepsilon}\Big(& C_{19}kS^2Sr{Y_1}^2 - C_{18}kS^2Sr{Y_1}^3 + C_{19}kS^2SrY_1Y_2 - C_{18}kS^2Sr{Y_1}^2Y_2 + S^2{Y_1}^2\varepsilon \\
& + 2S^2Y_1Y_2\varepsilon + S^2{Y_2}^2\varepsilon - A_3\text{Da}S^2Y_1Y_2\gamma\varepsilon - C_{13}kS^2SrY_1\cosh(SY_1) \\
& - C_{13}kS^2SrY_2\cosh(SY_1) - 2A_1A_3\gamma\varepsilon\cosh(SY_1) - C_{12}kS^2SrY_1\cosh(2SY_1) \\
& - C_{12}kS^2SrY_2\cosh(2SY_1) - 2A_2A_3SY_1\gamma\varepsilon\cosh\left(\frac{1}{2}S(-Y_1 + Y_2)\right) \\
& - C_{14}kS^2SrY_1\cosh(\alpha Y_1) - C_{14}kS^2SrY_2\cosh(\alpha Y_1) + C_{16}kS^2SrY_1\sinh(SY_1) \\
& + C_{16}kS^2SrY_2\sinh(SY_1) + 2A_2A_3\gamma\varepsilon\sinh(SY_1) + C_{15}kS^2SrY_1\sinh(2SY_1) \\
& + C_{15}kS^2SrY_2\sinh(2SY_1) - 2A_1A_3SY_1\gamma\varepsilon\sinh\left(\frac{1}{2}S(-Y_1 + Y_2)\right) \\
& + C_{17}kS^2SrY_1\sinh(\alpha Y_1) + C_{17}kS^2SrY_2\sinh(\alpha Y_1)\Big).
\end{aligned}
$$

(A4i)

Appendix B: Validation

B1. Analytical validation

To validate the mathematical model developed in Section 3, it is demonstrated that when the wall thicknesses are equal and there is no exothermic catalytic reaction, the temperature fields reduce to that presented by Hunt et al. [17] and Ting et al. [38]. To produce a system equivalent to that of Ref. [17], we set $h_1 = h_2$. It is also necessary to reverse the directions of q_{w1} and q_{w2} and set their magnitudes equal to q_1 and q_2 respectively, which in terms

of non-dimensional parameters leads to $Q_{w1} = 2(Q-1)$ and $Q_{w2} = -2Q$. Accounting for the difference in parameter definitions of Br', Re and θ_i then the axial thermal gradient, Eq (17) becomes:

$$\theta_i(X) = \frac{X\left[1 + A_4' Br'\right]}{2Re\,\Pr k\,Y_1 \xi} \qquad i = 1,2,s,f \tag{B1}$$

where,

$$A_4' = \frac{2S^3 Y_1{}^2 \cosh(SY_1)}{S\,Y_1 \cosh(SY_1) - \sinh(SY_1)}. \tag{B2}$$

This is the same as the axial thermal gradient found by Hunt et al. [17] where A_4' represents the coefficient of the modified Brinkman number. Next, the radial thermal equations can be determined from Eqs, (18b) and (18c) using the given conditions to yield the coupled equations:

$$k\theta_f'' + Bi\left(\theta_s - \theta_f\right) + B_1' \cosh(2SY) + B_2' \sinh(2SY) + B_3' \cosh(SY) \qquad\qquad -Y_1 \leq Y < Y_2 \tag{B3a}$$
$$+ B_4' \sinh(SY) + B_5' = 0$$

$$\theta_s'' - Bi\left(\theta_s - \theta_f\right) = 0 \qquad\qquad\qquad -Y_1 \leq Y < Y_2 \tag{B3b}$$

where, taking into consideration the difference in parameter definitions of Br' and θ_i , the modified coefficients (which are shown by use of a prime) are:

$$B_1' = \frac{Br' S^4 Y_1^2}{(SY_1 \cosh(SY_1) - \sinh(SY_1))^2}, \tag{B4a}$$

$$B_2' = 0, \tag{B4b}$$

$$B_3' = -\frac{S\,\mathrm{sech}(SY_1)\left[SY_1(2Br'S^2Y_1 - 1) + \tanh(SY_1)\right]}{2(-SY_1 + \tanh(SY_1))^2}, \tag{B4c}$$

$$B_4' = 0, \tag{B4d}$$

$$B_5' = -\frac{S}{SY_1 - \tanh(SY_1)}. \tag{B4e}$$

The coefficients $B_1' - B_4'$ once rearranged are identical to the equivalent coefficients calculated by Hunt et al. for the coupled thermal equations investigated therein under the previously stated conditions. Thus, the final fluid and porous solid thermal equations, Eqs. (20a) to (20d) under these conditions yield the followings.

$$\theta_2(Y) = C_1' + C_2'Y \qquad\qquad Y_2 < Y \leq 1 \tag{B5a}$$

$$\theta_s(Y) = C_3' \cosh(2SY) + C_4' \cosh(SY) + C_5' \cosh(\alpha Y) + C_6' \sinh(2SY) \qquad -Y_1 \leq Y < Y_2 \tag{B5b}$$
$$+ C_7' \sinh(SY) + C_8' \sinh(\alpha Y) + C_9'Y^2 + C_{10}'Y + C_{11}'$$

$$\theta_f(Y) = C_{12}' \cosh(2SY) + C_{13}' \cosh(SY) + C_{14}' \cosh(\alpha Y) + C_{15}' \sinh(2SY) \qquad -Y_1 \leq Y < Y_2 \tag{B5c}$$
$$+ C_{16}' \sinh(SY) + C_{17}' \sinh(\alpha Y) + C_{18}'Y^2 + C_{19}'Y + C_{20}'$$

$$\theta_1(Y) = C_{21}' + C_{22}'Y \qquad\qquad -1 \leq Y < -Y_1 \tag{B5d}$$

where the new coefficients are defined as:

$$C_1' = \frac{Y_2 Q_{w2}}{2k_{e2}} + \theta_{w2}', \qquad\qquad\qquad C_2' = -\frac{Q_{w2}}{k_{e2}}, \tag{B6a,b}$$

$$C_3' = \frac{B_1' Bi}{16kS^4 - 4kS^2\alpha^2}, \qquad\qquad C_4' = \frac{B_3' Bi}{kS^4 - kS^2\alpha^2}, \tag{B6c,d}$$

$$C_5' = \frac{1}{(k\alpha^4(4S^4 - 5S^2\alpha^2 + \alpha^4))} [Bi(B_3'\alpha^2(\alpha^2 - 4S^2)\cosh(SY_1) + (S^2 - \alpha^2)(4S^2 B_5' \tag{B6e}$$
$$- B_5'\alpha^2 - B_1'\alpha^2\cosh(2SY_1)))\operatorname{sech}(\alpha Y_1)],$$

$$C_6' = C_7' = C_8' = 0, \qquad\qquad C_9' = \frac{-B_5' Bi}{2k\alpha^2}, \tag{B6f,g}$$

$$C_{10}' = \frac{\theta_{w2}'}{2Y_1}, \tag{B6h}$$

$$C_{11}' = \frac{1}{2kS^2\alpha^4}[2S^2(B_5'Bi(Y_1^2\alpha^2 - 2) + k\alpha^4\theta_{w2}') \tag{B6i}$$
$$+ 4B_3'Bi\alpha^2\cosh(SY_1) + B_1'Bi\alpha^2\cosh(2SY_1)],$$

$$C_{12}' = \frac{B_1'(Bi - 4S^2)}{4kS^2(4S^2 - \alpha^2)}, \qquad\qquad C_{13}' = -\frac{B_3'(S^2 - Bi)}{kS^4 - kS^2\alpha^2}, \tag{B6j,k}$$

$$C_{14}' = \frac{1}{(k\alpha^4(4S^4 - 5S^2\alpha^2 + \alpha^4))} [(Bi - \alpha^2)(B_3'\alpha^2(\alpha^2 - 4S^2)\cosh(SY_1) \tag{B6l}$$
$$+ (S^2 - \alpha^2)(4S^2 B_5' - B_5'\alpha^2 - B_1'\alpha^2\cosh(2SY_1)))\operatorname{sech}(\alpha Y_1)],$$

$$C_{15}' = C_{16}' = C_{17}' = 0, \qquad\qquad C_{18}' = \frac{-B_5' Bi}{2k\alpha^2}, \tag{B6m,n}$$

$$C_{19}' = \frac{\theta_{w2}'}{2Y_1}, \tag{B6o}$$

$$C_{20}' = \frac{1}{4kS^2\alpha^4}[2S^2(B_5'Bi(Y_1^2\alpha^2 - 2) + k\alpha^4\theta_{w2}') \tag{B6p}$$
$$+ 4B_3'Bi\alpha^2\cosh(SY_1) + B_1'Bi\alpha^2\cosh(2SY_1)],$$

$$C_{21}' = \frac{Q_{w1}Y_1}{k_{e1}}, \qquad\qquad C_{22}' = \frac{Q_{w1}}{k_{e1}}. \tag{B6q,r}$$

With rearrangement of terms and taking into consideration the difference in parameter definitions of Br' and θ_i, the above coefficients show that Eqs. (B5a) to (B5d) are analytically identical to the thermal equations derived in the investigation by Hunt et al. [17], which itself could be rigorously reduced to the results of Ting et al. [38].

B2. Computational validation

For comparison purposes a model was developed in the computational multi-physics software, STAR-CCM+ of a microchannel 12mm in length, 800µm in height enclosed between walls of 50µm thickness. Steady, two-dimensional continuity, momentum and energy equations for the fluid and solid walls are solved on a grid consisting of 98344 cells.

Continuity equation:

$$\nabla \cdot (\rho \boldsymbol{v}) = 0. \tag{B2-a}$$

Momentum equation:

$$\nabla \cdot (\rho \boldsymbol{v} \otimes \boldsymbol{v}) = \nabla \cdot \boldsymbol{\sigma}. \tag{B2-b}$$

Energy equation:

$$\nabla \cdot (\rho E \boldsymbol{v}) = \nabla \cdot (\boldsymbol{v} \cdot \boldsymbol{\sigma}) - \nabla \cdot \boldsymbol{q} + S_E. \tag{B2-c}$$

where; $\otimes$ represents the Kronecker product, $\boldsymbol{\sigma}$ is the stress tensor, E is the total energy per unit mass, $\boldsymbol{q}$ is the heat flux and S_E is an energy source term.

Grid independency tests confirmed the adequacy of this grid. Standard no slip velocity and no jump temperature boundary conditions were implemented. Using an interface between the walls and the fluid flowing within the microchannel the thermal specification of conjugate heat transfer was applied. A heat source interface was implemented at the boundary between each wall and the fluid within the microchannel. The heat flux into the wall and into the fluid from this heat source was measured. Thermal conductivity within the walls was set to 18 WK^{-1}m^{-1} to represent a ceramic and the fluid chosen was considered to be water. A mass flow rate was calculated to give a Reynolds number of 7. These figures permitted the development of an analytical model using the temperature equations derived in Section 3, using a porosity of 0.999, and a Darcy number of 1000 to represent the flow inside a clear conduit. The analytically and computationally predicted temperature fields are shown in Fig. B1, featuring a good agreement. Further, for the configuration shown in Fig. B1, the Nusselt number calculated by Eq. (32) is 4.29 and that obtained computationally is 4.45. Once again, this shows an excellent agreement between the two models. It is worth recalling that consideration of a clear microchannel (instead of a porous one) was to avoid using any interface model on the surface of the walls.

References
[1] N. Kockmann, Transport phenomena in micro process engineering, Springer, 2008.
[2] S.M. Peyghambarzadeh, S.H. Hashemabadi, A.R. Chabi, M. Salimi, Performance of water based CuO and Al2O3 nanofluids in a Cu–Be alloy heat sink with rectangular microchannels, Energy Convers. Manag. 86 (2014) 28–38. doi:10.1016/J.ENCONMAN.2014.05.013.
[3] P.-X. Jiang, M.-H. Fan, G.-S. Si, Z.-P. Ren, Thermal–hydraulic performance of small scale micro-channel and porous-media heat-exchangers, Int. J. Heat Mass Transf. 44 (2001) 1039–1051. doi:10.1016/S0017-9310(00)00169-1.
[4] T.-C. Hung, W.-M. Yan, Thermal Performance Enhancement of Microchannel Heat Sinks with Sintered Porous Media, Numer. Heat Transf. Part A Appl. 63 (2013) 666–686. doi:10.1080/10407782.2013.751778.
[5] G. Kolb, V. Hessel, Micro-structured reactors for gas phase reactions, Chem. Eng. J. 98 (2004) 1–38. doi:10.1016/j.cej.2003.10.005.
[6] J.-I. Yoshida, A. Nagaki, T. Iwasaki, S. Suga, Enhancement of Chemical Selectivity by Microreactors, (n.d.). doi:10.1002/ceat.200407127.
[7] T. Fukuyama, Y. Hino, N. Kamata, I. Ryu, Quick Execution of [2+2] Type Photochemical Cycloaddition Reaction by Continuous Flow System Using a Glass-made Microreactor, Chem. Lett. 33 (2004) 1430–1431. doi:10.1246/cl.2004.1430.
[8] T. Wirth, Microreactors in Organic Chemistry and Catalysis, (2013) 470.
[9] M. Götz, J. Lefebvre, F. Mörs, A. McDaniel Koch, F. Graf, S. Bajohr, R. Reimert, T. Kolb, Renewable Power-to-Gas: A technological and economic review, Renew. Energy. 85 (2016) 1371–1390. doi:10.1016/J.RENENE.2015.07.066.
[10] G. Kolb, Review: Microstructured reactors for distributed and renewable production of fuels and electrical energy, Chem. Eng. Process. Process Intensif. 65 (2013) 1–44. doi:10.1016/j.cep.2012.10.015.
[11] H. Pennemann, G. Kolb, Review: Microstructured reactors as efficient tool for the operation of selective oxidation reactions, Catal. Today. 278 (2016) 3–21. doi:10.1016/J.CATTOD.2016.04.032.
[12] H. Ammar, B. Garnier, A. Ould el Moctar, H. Willaime, F. Monti, H. Peerhossaini, Thermal analysis of chemical reactions in microchannels using highly sensitive thin-film heat-flux microsensor, Chem. Eng. Sci. 94 (2013) 150–155. doi:10.1016/j.ces.2013.02.055.
[13] R. Sui, N.I. Prasianakis, J. Mantzaras, N. Mallya, J. Theile, D. Lagrange, M. Friess, An experimental and numerical investigation of the combustion and heat transfer characteristics of hydrogen-fueled catalytic microreactors, Chem. Eng. Sci. 141 (2016) 214–230. doi:10.1016/j.ces.2015.10.034.

[14] N.S. Kaisare, D.G. Vlachos, A review on microcombustion: Fundamentals, devices and applications, Prog. Energy Combust. Sci. 38 (2012) 321–359. doi:10.1016/j.pecs.2012.01.001.

[15] M.J. Stutz, D. Poulikakos, Effects of microreactor wall heat conduction on the reforming process of methane, Chem. Eng. Sci. 60 (2005) 6983–6997. doi:10.1016/j.ces.2005.06.012.

[16] G. Hunt, M. Torabi, L. Govone, N. Karimi, A. Mehdizadeh, Two-dimensional heat and mass transfer and thermodynamic analyses of porous microreactors with Soret and thermal radiation effects—An analytical approach, Chem. Eng. Process. - Process Intensif. 126 (2018). doi:10.1016/j.cep.2018.02.025.

[17] G. Hunt, N. Karimi, M. Torabi, Two-dimensional analytical investigation of coupled heat and mass transfer and entropy generation in a porous, catalytic microreactor, Int. J. Heat Mass Transf. 119 (2018). doi:10.1016/j.ijheatmasstransfer.2017.11.118.

[18] G. Hunt, N. Karimi, M. Torabi, Analytical investigation of heat transfer and classical entropy generation in microreactors – The influences of exothermicity and asymmetry, Appl. Therm. Eng. 119 (2017) 403–424. doi:10.1016/j.applthermaleng.2017.03.057.

[19] M. Torabi, A. Elliott, N.K. Karimi, Thermodynamics analyses of porous microchannels with asymmetric thick walls and exothermicity: An entropic model of micro-reactors, J. Therm. Sci. Eng. Appl. (2017). doi:10.1115/1.4036802.

[20] S.-X. Zhang, Y.-L. He, G. Lauriat, W.-Q. Tao, Numerical studies of simultaneously developing laminar flow and heat transfer in microtubes with thick wall and constant outside wall temperature, Int. J. Heat Mass Transf. 53 (2010) 3977–3989. doi:10.1016/j.ijheatmasstransfer.2010.05.017.

[21] G. Ibáñez, A. López, J. Pantoja, J. Moreira, J.A. Reyes, Optimum slip flow based on the minimization of entropy generation in parallel plate microchannels, Energy. 50 (2013) 143–149. doi:10.1016/j.energy.2012.11.036.

[22] M. Torabi, G.P. Peterson, Effects of velocity slip and temperature jump on the heat transfer and entropy generation in micro porous channels under magnetic field, Int. J. Heat Mass Transf. 102 (2016) 585–595. doi:10.1016/j.ijheatmasstransfer.2016.06.080.

[23] M. Torabi, K. Zhang, N. Karimi, G.P. Peterson, Entropy generation in thermal systems with solid structures – A concise review, Int. J. Heat Mass Transf. 97 (2016) 917–931. doi:10.1016/j.ijheatmasstransfer.2016.03.007.

[24] Y. Mahmoudi, N. Karimi, K. Mazaheri, Analytical investigation of heat transfer enhancement in a channel partially filled with a porous material under local thermal non-equilibrium condition: Effects of different thermal boundary conditions at the porous-fluid interface, Int. J. Heat Mass Transf. 70 (2014) 875–891. doi:10.1016/J.IJHEATMASSTRANSFER.2013.11.048.

[25] N. Karimi, D. Agbo, A. Talat Khan, P.L. Younger, On the effects of exothermicity and endothermicity upon the temperature fields in a partially-filled porous channel, Int. J. Therm. Sci. 96 (2015) 128–148. doi:10.1016/j.ijthermalsci.2015.05.002.

[26] G. Hunt, N. Karimi, M. Torabi, Analytical investigation of heat transfer and classical entropy generation in microreactors – The influences of exothermicity and asymmetry, Appl. Therm. Eng. 119 (2017). doi:10.1016/j.applthermaleng.2017.03.057.

[27] A. Elliott, M. Torabi, N. Karimi, S. Cunningham, On the effects of internal heat sources upon forced convection in porous channels with asymmetric thick walls, Int. Commun. Heat Mass Transf. 73 (2016) 100–110. doi:10.1016/j.icheatmasstransfer.2016.02.016.

[28] J. Koo, C. Kleinstreuer, Viscous dissipation effects in microtubes and microchannels, Int. J. Heat Mass Transf. 47 (2004) 3159–3169. doi:10.1016/J.IJHEATMASSTRANSFER.2004.02.017.

[29] G.L. Morini, Viscous heating in liquid flows in micro-channels, Int. J. Heat Mass Transf. 48 (2005) 3637–3647. doi:10.1016/J.IJHEATMASSTRANSFER.2005.01.011.

[30] Y.M. Hung, Analytical Study on Forced Convection of Nanofluids With Viscous Dissipation in Microchannels, Heat Transf. Eng. 31 (2010) 1184–1192. doi:10.1080/01457631003689344.

[31] G.M. Chen, C.P. Tso, Forced convection with viscous dissipation using a two-equation model in a channel filled by a porous medium, Int. J. Heat Mass Transf. 54 (2011) 1791–1804. doi:10.1016/j.ijheatmasstransfer.2010.12.037.

[32] N. Verma, D. Mewes, A. Luke, Lattice Boltzmann study of velocity, temperature, and concentration in micro-reactors, Int. J. Heat Mass Transf. 53 (2010) 3175–3185. doi:10.1016/j.ijheatmasstransfer.2010.03.009.

[33] W.M. Deen, Analysis of transport phenomena, Oxford University Press, 1998.

[34] M.H. Matin, I. Pop, Forced convection heat and mass transfer flow of a nanofluid through a porous channel with a first order chemical reaction on the wall, Int. Commun. Heat Mass Transf. 46 (2013) 134–141. doi:10.1016/j.icheatmasstransfer.2013.05.001.

[35] A. Bejan, Fundamentals of exergy analysis, entropy generation minimization, and the generation of flow architecture, Int. J. Energy Res. (2002).

[36] M. Torabi, M. Torabi, G.P. Peterson, Entropy Generation of Double Diffusive Forced Convection in Porous

Channels with Thick Walls and Soret Effect, Entropy. 19 (2017) 171. doi:10.3390/e19040171.

[37] T.W. Ting, Y.M. Hung, N. Guo, Entropy generation of viscous dissipative nanofluid flow in thermal non-equilibrium porous media embedded in microchannels, Int. J. Heat Mass Transf. 81 (2015) 862–877. doi:10.1016/j.ijheatmasstransfer.2014.11.006.

[38] T.W. Ting, Y.M. Hung, N. Guo, Entropy generation of viscous dissipative nanofluid convection in asymmetrically heated porous microchannels with solid-phase heat generation, Energy Convers. Manag. 105 (2015) 731–745. doi:10.1016/j.enconman.2015.08.022.

[39] C. Dickson, M. Torabi, N. Karimi, First and second law analyses of nanofluid forced convection in a partially-filled porous channel – The effects of local thermal non-equilibrium and internal heat sources, Appl. Therm. Eng. 103 (2016) 459–480. doi:10.1016/j.applthermaleng.2016.04.095.

[40] M. Torabi, C. Dickson, N. Karimi, Theoretical investigation of entropy generation and heat transfer by forced convection of copper–water nanofluid in a porous channel — Local thermal non-equilibrium and partial filling effects, Powder Technol. 301 (2016) 234–254. doi:10.1016/j.powtec.2016.06.017.

[41] M. Kaviany, Principles of heat transfer in porous media, 2012.

[42] D. Nield, A. Bejan, Convection in Porous Media, (2013).

[43] K. Vafai, Handbook of porous media, 2015.

[44] B. Alazmi, K. Vafai, Constant wall heat flux boundary conditions in porous media under local thermal non-equilibrium conditions, Int. J. Heat Mass Transf. 45 (2002) 3071–3087. doi:10.1016/S0017-9310(02)00044-3.

[45] D.-Y. Lee, K. Vafai, Analytical characterization and conceptual assessment of solid and fluid temperature differentials in porous media, Int. J. Heat Mass Transf. 42 (1999) 423–435. doi:10.1016/S0017-9310(98)00185-9.

[46] K. Yang, K. Vafai, Analysis of temperature gradient bifurcation in porous media – An exact solution, Int. J. Heat Mass Transf. 53 (2010) 4316–4325. doi:10.1016/j.ijheatmasstransfer.2010.05.060.

[47] Y. Mahmoudi, N. Karimi, Numerical investigation of heat transfer enhancement in a pipe partially filled with a porous material under local thermal non-equilibrium condition, Int. J. Heat Mass Transf. 68 (2014) 161–173. doi:10.1016/j.ijheatmasstransfer.2013.09.020.

[48] M. Torabi, N. Karimi, K. Zhang, G.P. Peterson, Generation of entropy and forced convection of heat in a conduit partially filled with porous media – Local thermal non-equilibrium and exothermicity effects, Appl. Therm. Eng. 106 (2016) 518–536. doi:10.1016/j.applthermaleng.2016.06.036.

[49] R.-Y. Chein, L.-C. Chen, Y.-C. Chen, J.N. Chung, Heat transfer effects on the methanol-steam reforming with partially filled catalyst layers, Int. J. Hydrogen Energy. 34 (2009) 5398–5408. doi:10.1016/j.ijhydene.2009.04.049.

[50] R.-Y. Chein, Y.-C. Chen, J.N. Chung, Thermal resistance effect on methanol-steam reforming performance in micro-scale reformers, Int. J. Hydrogen Energy. 37 (2012) 250–262. doi:10.1016/j.ijhydene.2011.09.070.

[51] Y. Wenming, J. Dongyue, C.K.Y. Kenny, Z. Dan, P. Jianfeng, Combustion process and entropy generation in a novel microcombustor with a block insert, Chem. Eng. J. 274 (2015) 231–237. doi:10.1016/j.cej.2015.04.034.

[52] U. Rana, S. Chakraborty, S.K. Som, Thermodynamics of premixed combustion in a heat recirculating micro combustor, Energy. 68 (2014) 510–518. doi:10.1016/j.energy.2014.02.070.

[53] V. Hessel, A. Renken, J.C. Schouten, J.-I. Yoshida, eds., Micro Process Engineering, Wiley-VCH Verlag GmbH & Co. KGaA, Weinheim, Germany, 2009. doi:10.1002/9783527631445.

[54] T.W. Ting, Y.M. Hung, N. Guo, Viscous dissipative forced convection in thermal non-equilibrium nanofluid-saturated porous media embedded in microchannels, Int. Commun. Heat Mass Transf. 57 (2014) 309–318. doi:10.1016/j.icheatmasstransfer.2014.08.018.

[55] R.C. Givler, S.A. Altobelli, A determination of the effective viscosity for the Brinkman–Forchheimer flow model, J. Fluid Mech. 258 (1994) 355. doi:10.1017/S0022112094003368.

[56] K. Hooman, A. Ejlali, Entropy generation for forced convection in a porous saturated circular tube with uniform wall temperature, Int. Commun. Heat Mass Transf. 34 (2007) 408–419. doi:10.1016/j.icheatmasstransfer.2006.10.008.

[57] F.P. Incropera, D.P. DeWitt, T.L. Bergman, A.S. Lavine, Fundamentals of Heat and Mass Transfer, John Wiley & Sons, 2007. doi:10.1016/j.applthermaleng.2011.03.022.

[58] T.W. Ting, Y.M. Hung, N. Guo, Entropy generation of nanofluid flow with streamwise conduction in microchannels, Energy. 64 (2014) 979–990. doi:10.1016/j.energy.2013.10.064.

[59] G.R. Kefayati, Simulation of double diffusive natural convection and entropy generation of power-law fluids in an inclined porous cavity with Soret and Dufour effects (Part II: Entropy generation), Int. J. Heat Mass Transf. 94 (2016) 582–624. doi:10.1016/J.IJHEATMASSTRANSFER.2015.11.043.

[60] M. Torabi, N. Karimi, K. Zhang, Heat transfer and second law analyses of forced convection in a channel partially filled by porous media and featuring internal heat sources, Energy. 93 (2015) 106–127.
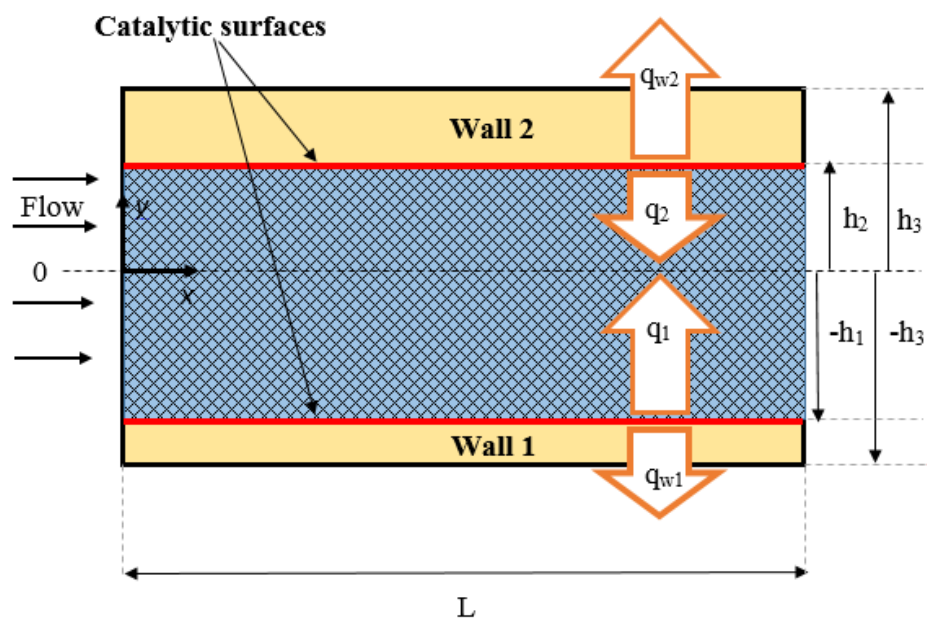
Figures and Tables

Fig 1. Schematic view of the microreactor under investigation.
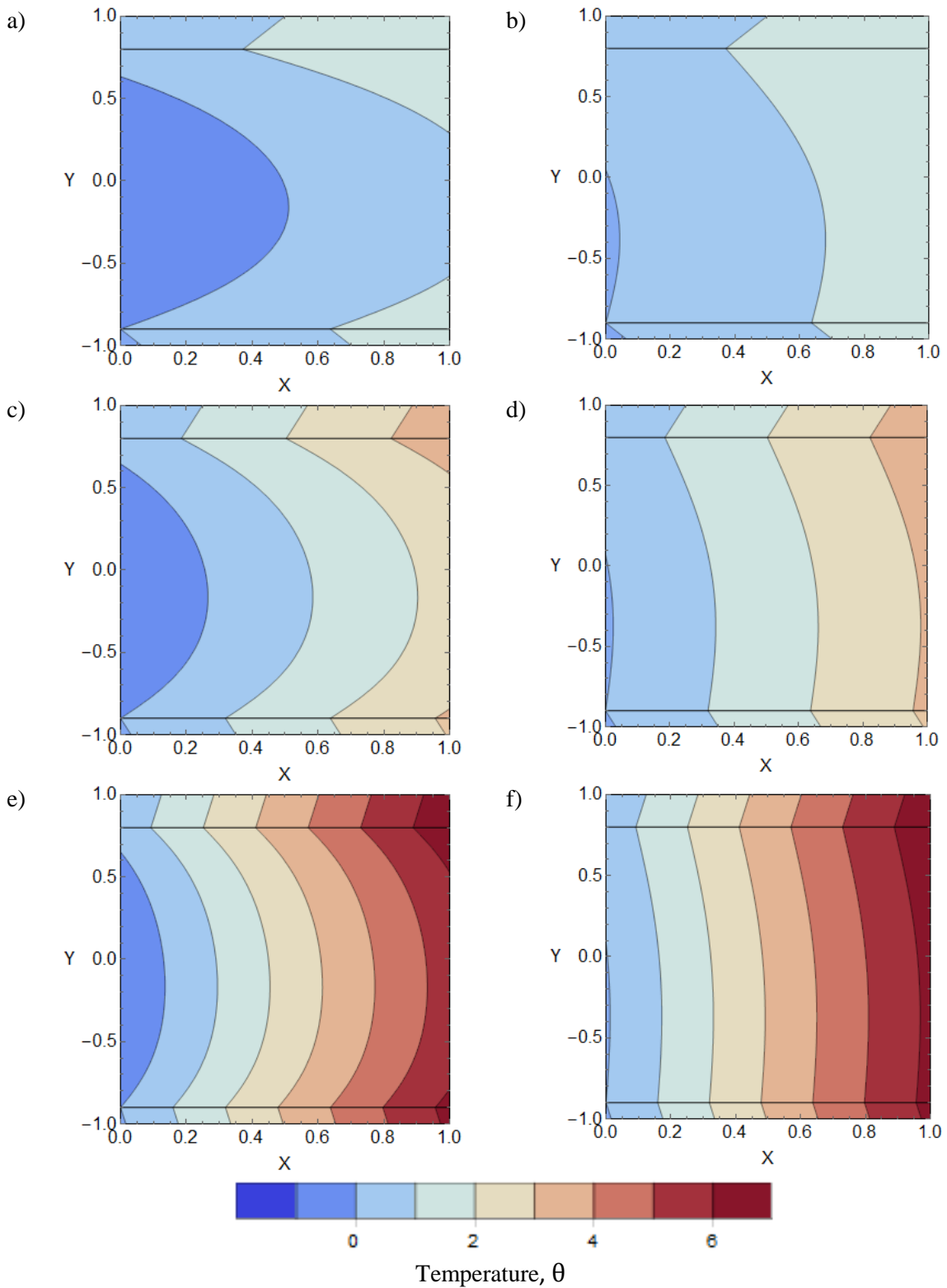
Fig 2. Dimensionless temperature contours for varying thermal conductivity ratio, k for the fluid and porous solid phase. Fluid phase is shown in a), c), and e) and solid phase is shown in b), d), and f) with $k = 0.02, 0.01, 0.005$, respectively.
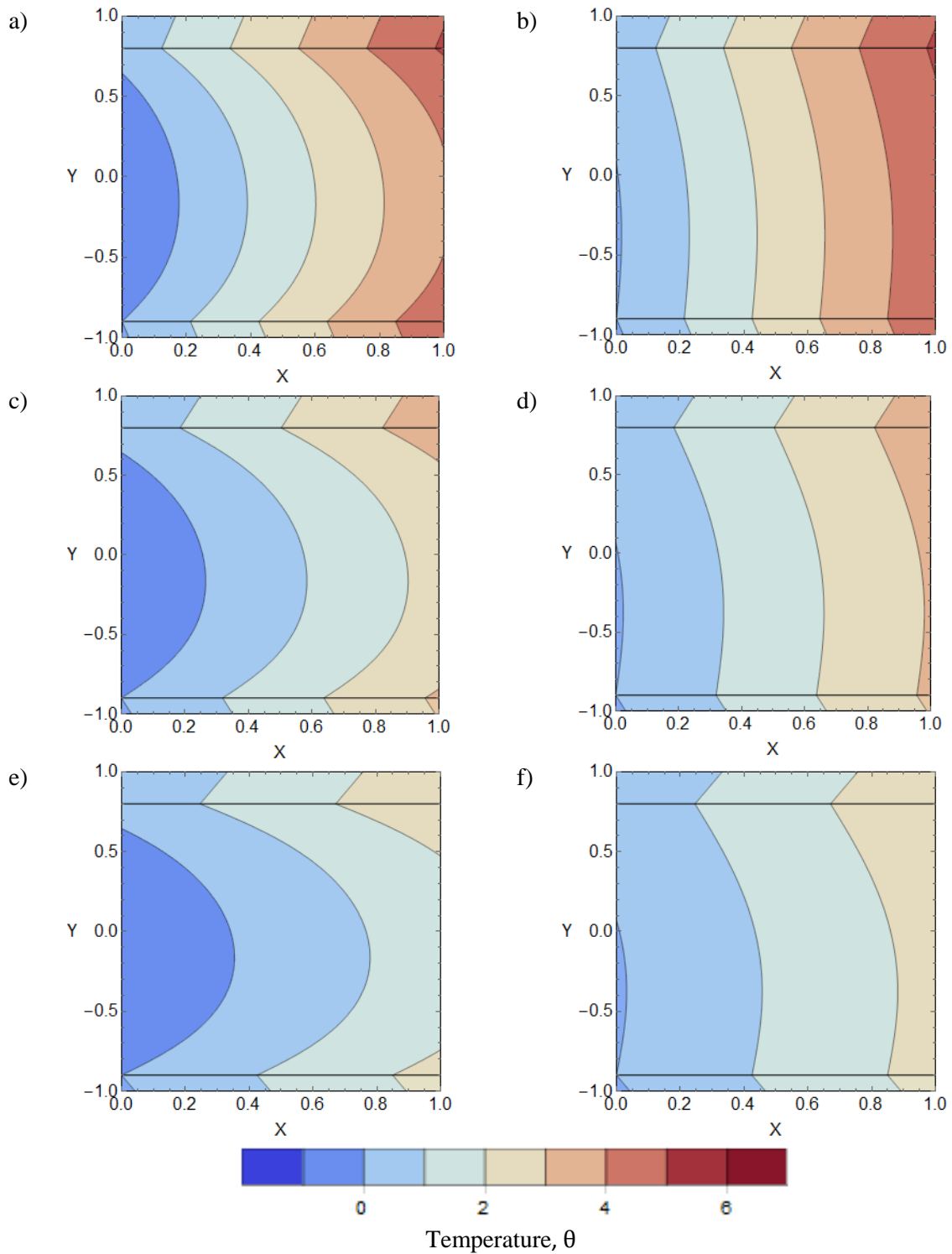
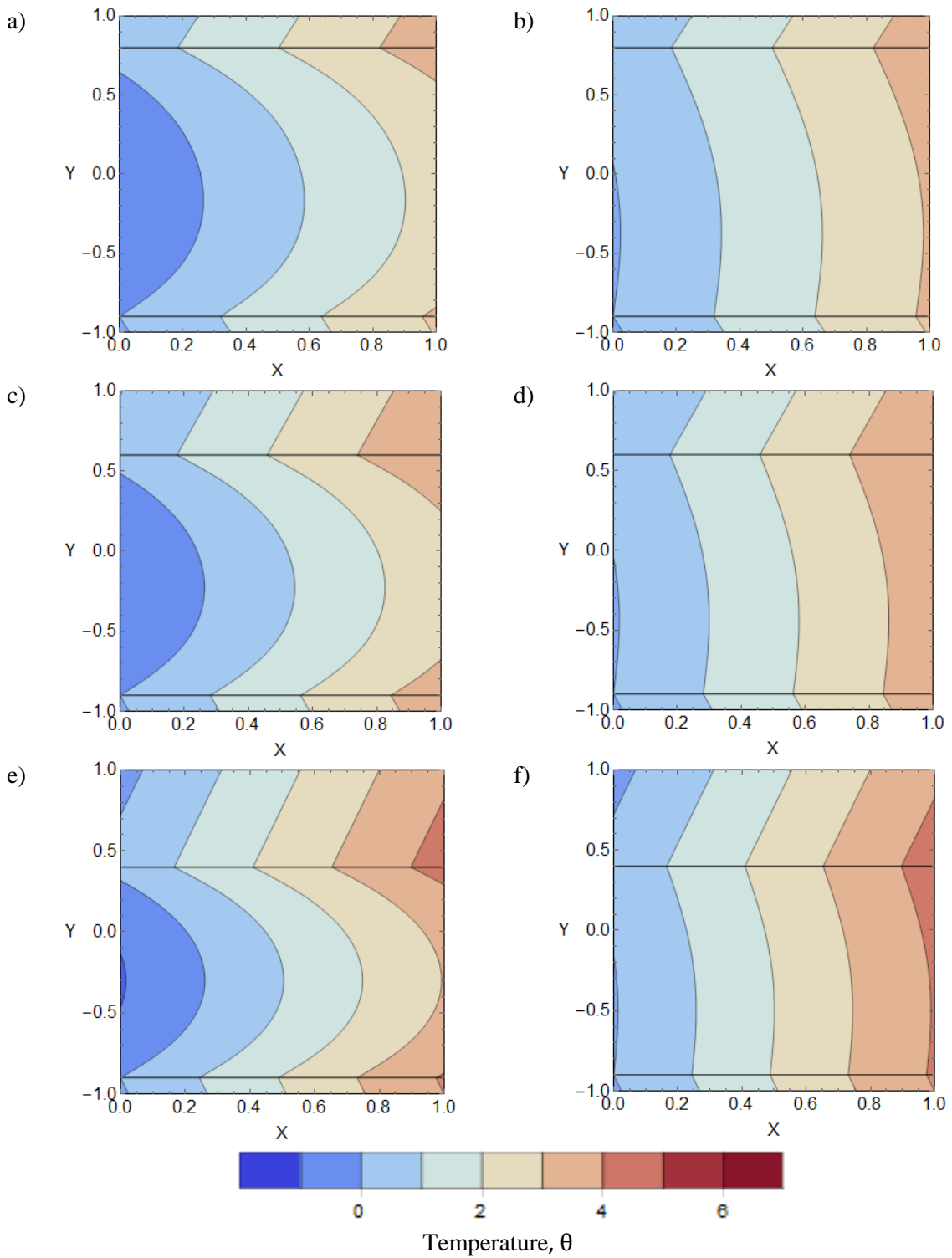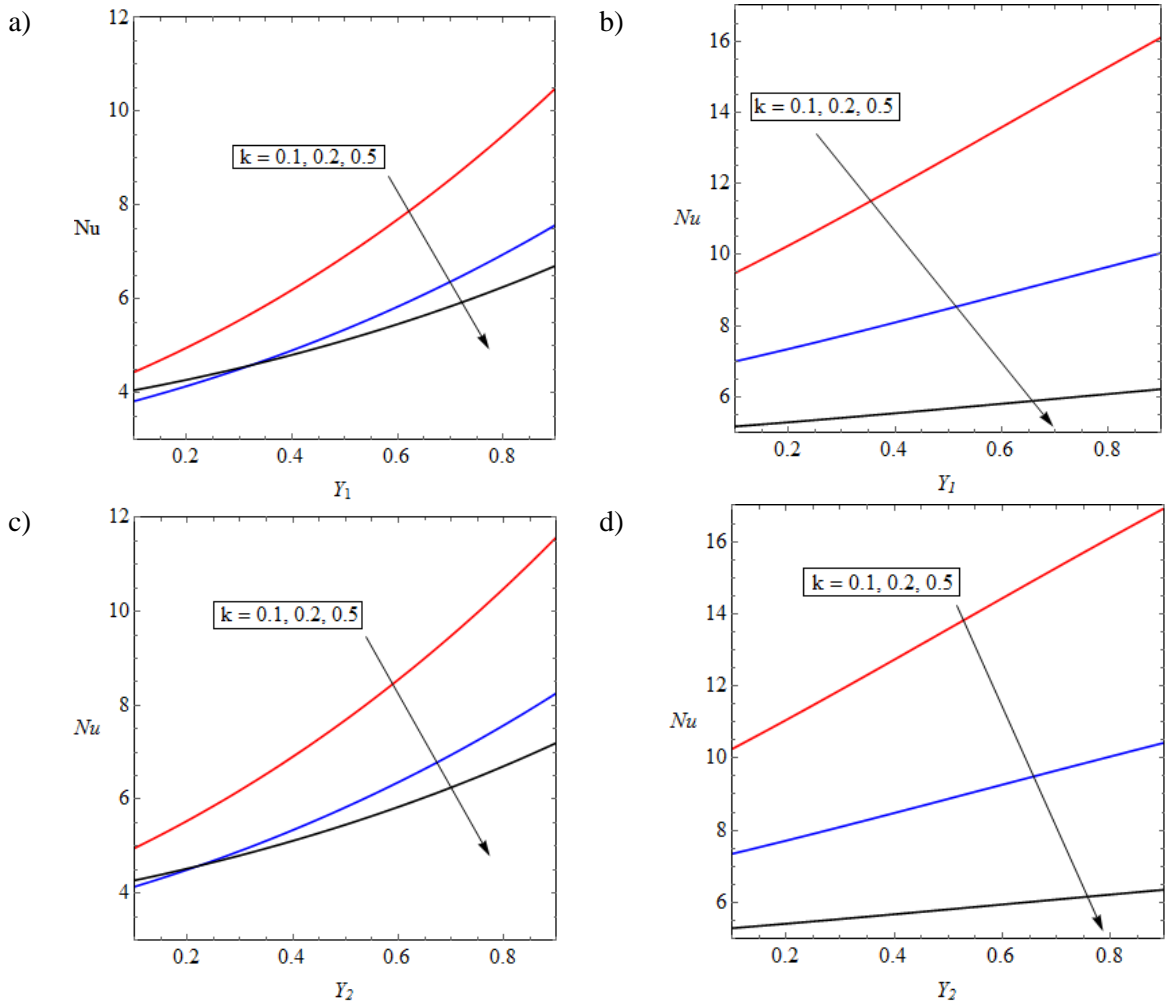**Fig 3**. Dimensionless temperature contours for varying Reynolds number, Re. Fluid phase is shown in a), c), and e) and solid phase is shown in b), d), and f) with Re = 50, 75, 100, respectively.

Fig 4. Dimensionless temperature contours for varying upper wall thickness, Y_2. Fluid phase is shown in a), c), and e) and solid phase is shown in b), d), and f) with $Y_2 = 0.8, 0.6, 0.4,$ respectively.

Fig 5. Variation of Nusselt number versus the lower and upper wall thicknesses, Y_1 & Y_2, for different values of thermal conductivity ratio, k, at a) & c) the lower wall and b) & d) the upper wall.
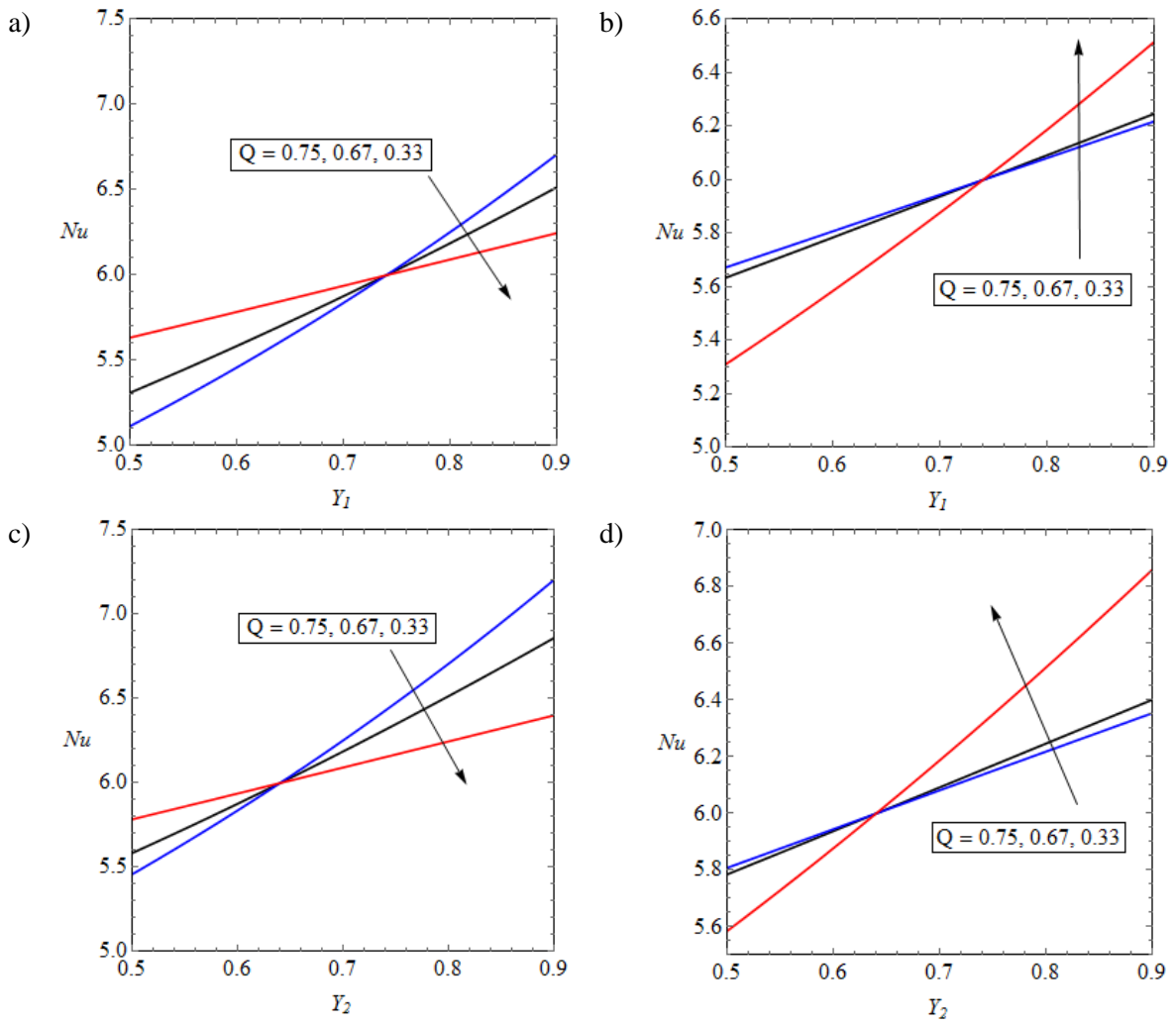
Fig 6. Variation of Nusselt number versus the lower and upper wall thicknesses, Y_1 & Y_2, (k = 0.5) for different values of heat flux ratio, Q at a & c) the lower wall and b & d) the upper wall.
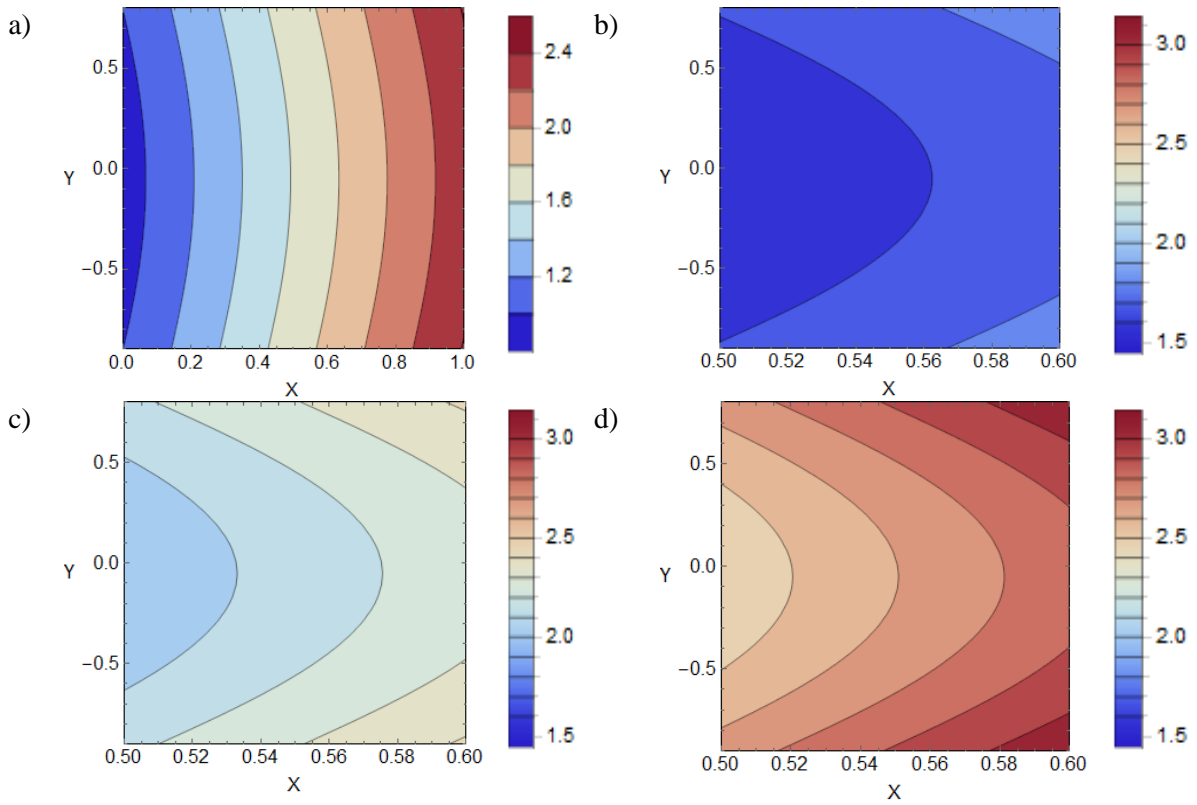
Fig 7. Dimensionless concentration contours for varying Damköhler number, γ a) showing the full microchannel for γ = 0.3, b) mid-section of channel, for γ = 0.3, c) mid-section for γ = 0.5, and d) mid-section for γ = 0.7.
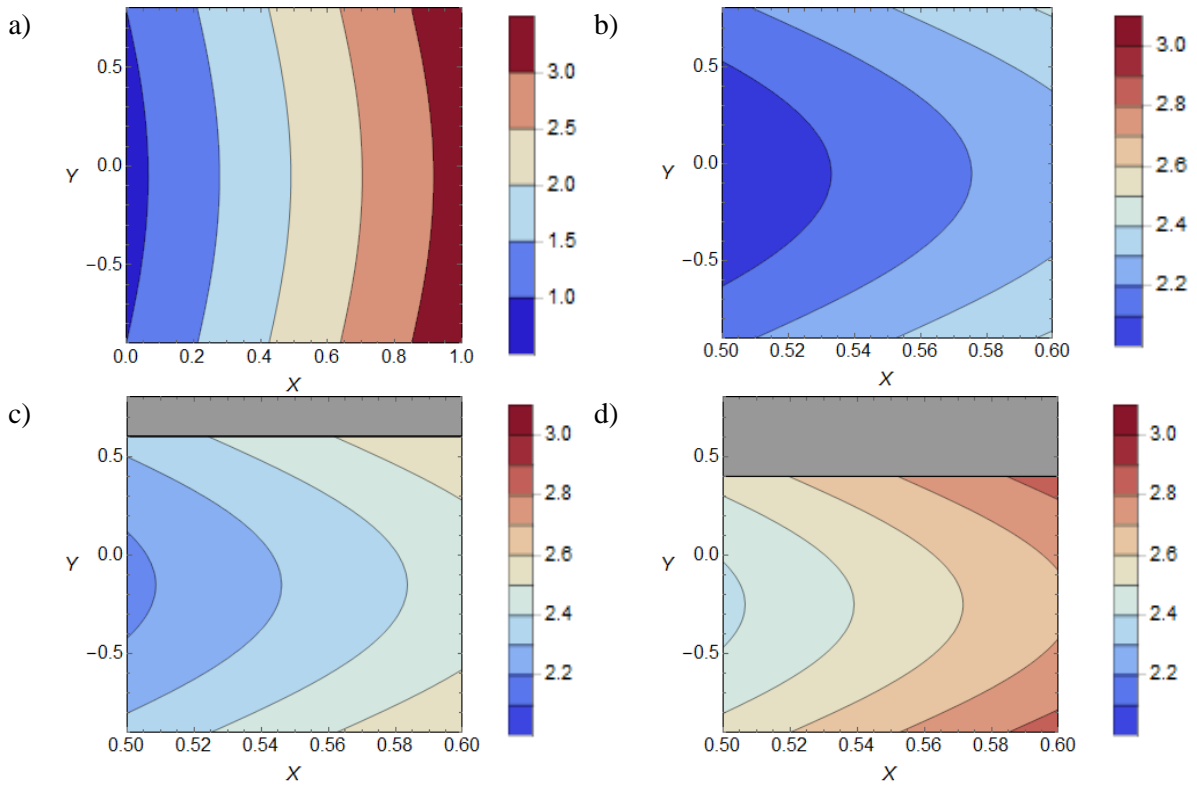
Fig 8. Dimensionless concentration contours for varying upper wall thickness, Y_2 a) showing the full microchannel for $Y_2 = 0.8$, b) mid-section of channel, for $Y_2 = 0.8$, c) mid-section for $Y_2 = 0.6$, and d) mid-section for $Y_2 = 0.4$.
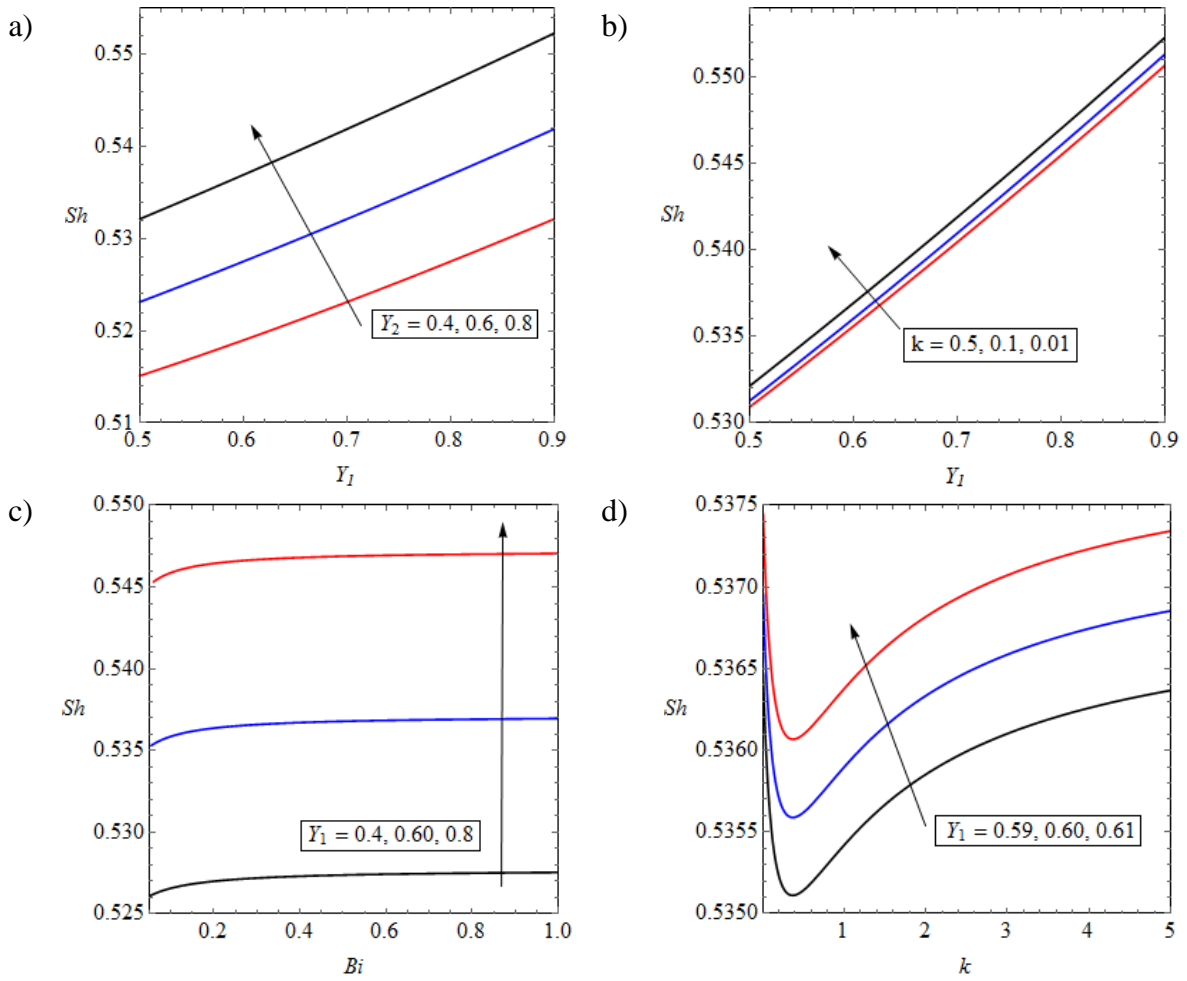
Fig 9. Variation in *Sh* versus the a) lower wall thickness, Y_1 for different values of upper wall thickness, Y_2 ,
b) lower wall thickness, Y_1 for different values of thermal conductivity ratio, k ,
c) Biot Number, Bi for different values of lower wall thickness, Y_1 and
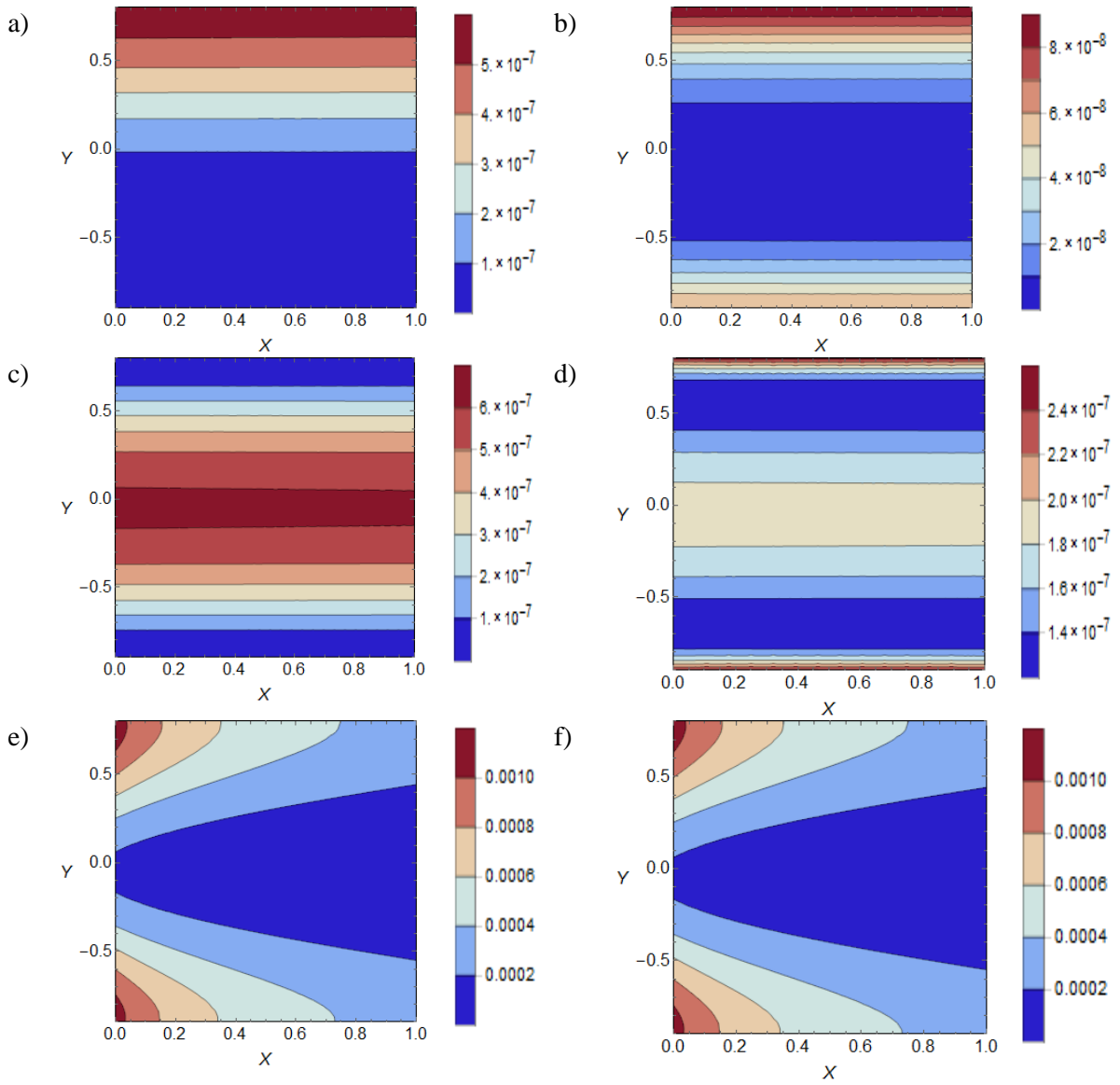d) thermal conductivity ratio, k for different values of lower wall thickness, Y_1.

Fig 10. Local entropy generation contours for the base configuration showing a)$N_{s,ht}$, b) $N_{f,ht}$, c) N_{int}, d)N_{FF}, e) N_{DI} and f) N_{PM}.
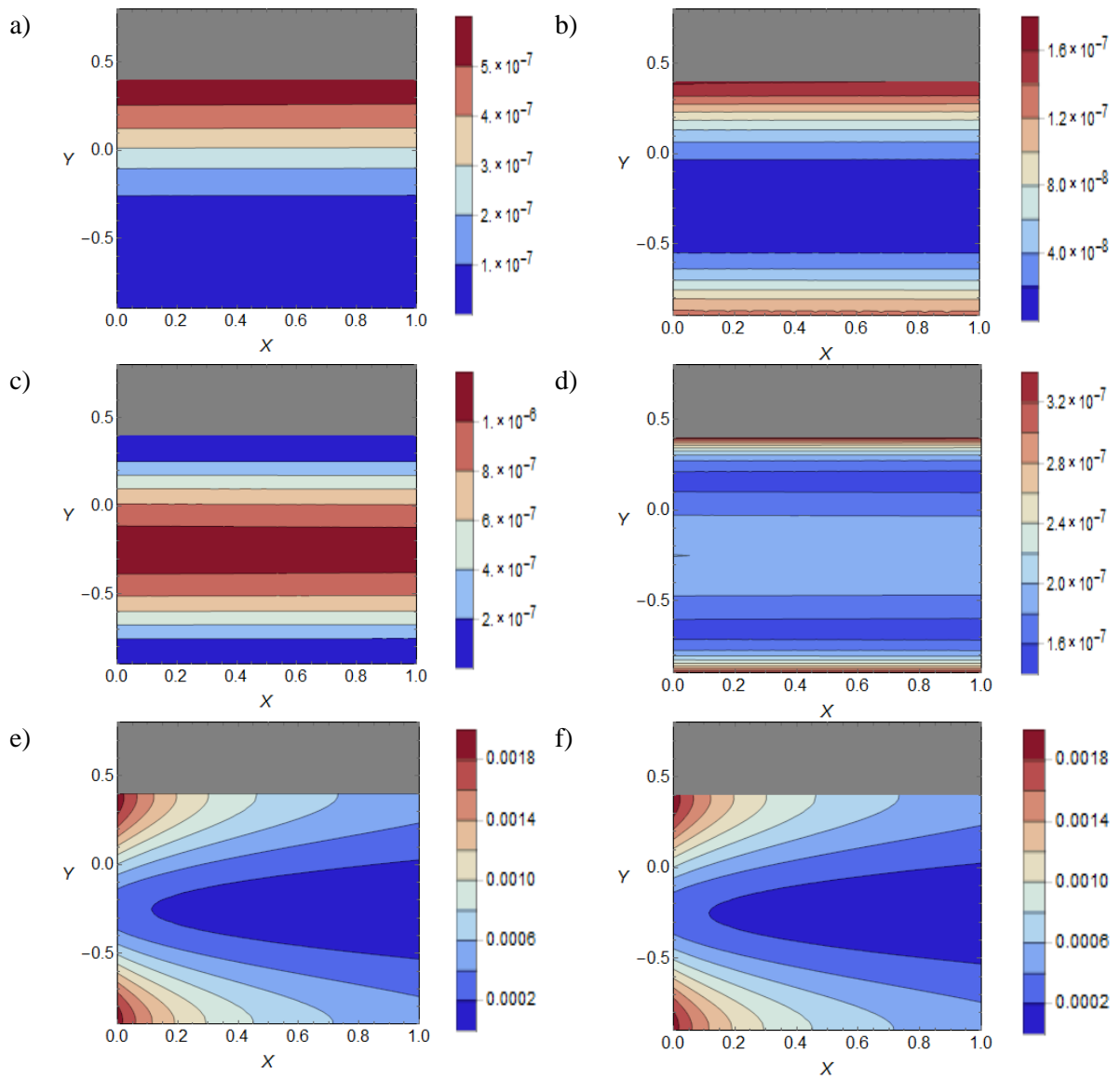
Fig 11. Local entropy generation contours for the upper wall thickness, $Y_2 = 0.4$ showing a) $N_{s,ht}$, b) $N_{f,ht}$, c) N_{int}, d) N_{FF}, e) N_{DI} and f) N_{PM}. The upper wall is coloured in grey to maintain the position of the central axis.
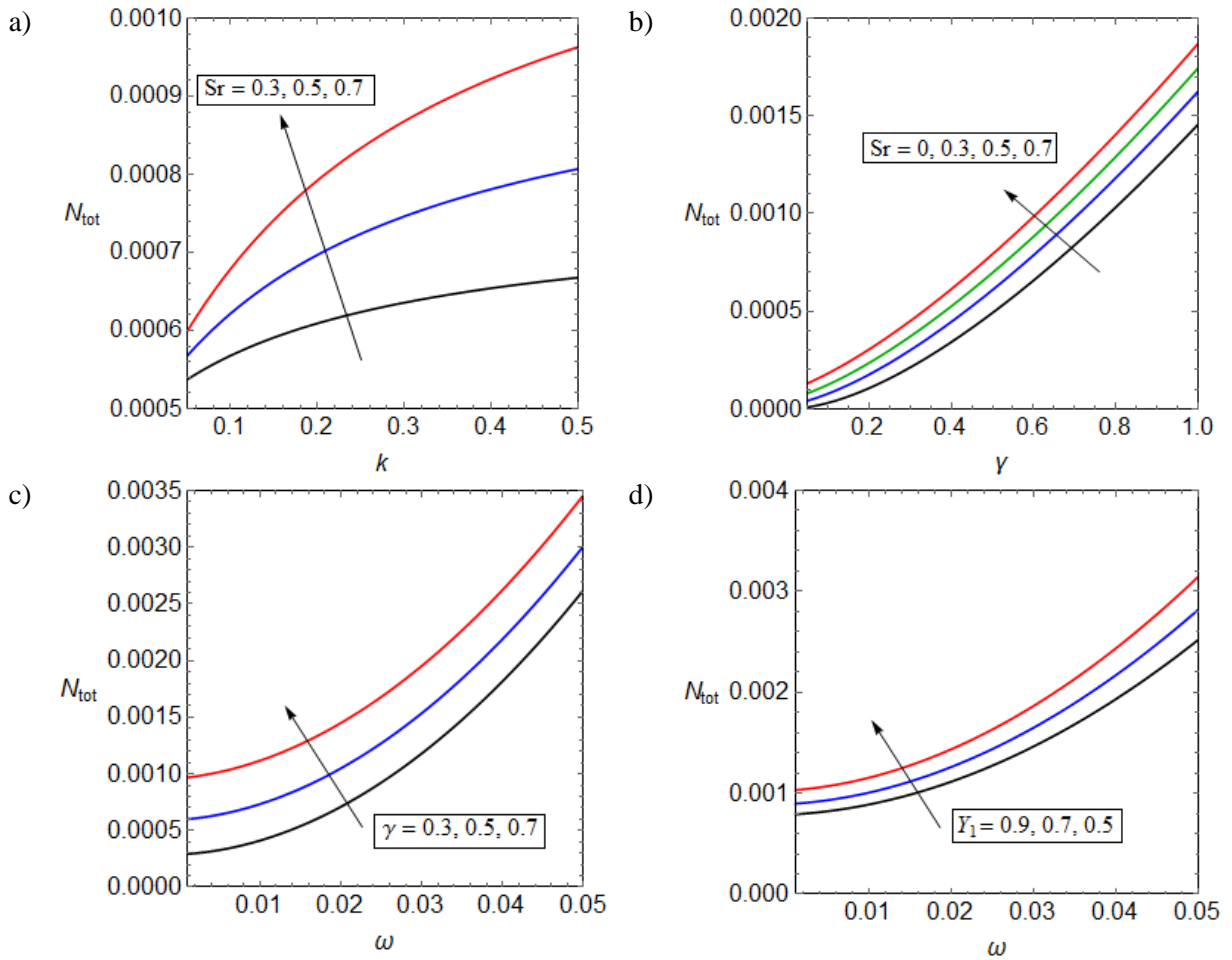
Fig 12. Total entropy generation for a) varying thermal conductivity ratio, k with different values of Soret number, Sr and b) varying Damköhler number, γ with different values of Soret number, Sr, and varying heat flux, ω with different values of c) Damköhler number, γ and d) for various values of Y_1.
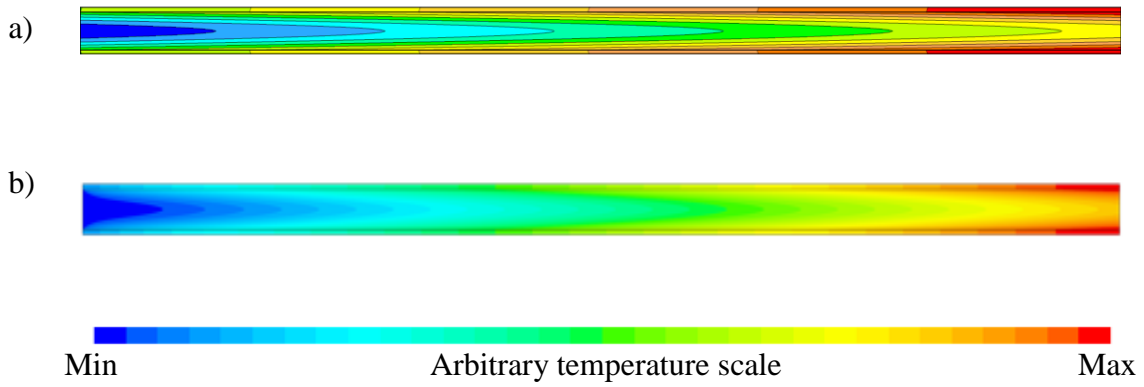
a)

b)

Min — Arbitrary temperature scale — Max

Fig B1. Comparison between the temperature fields in the microreactor, predicted
a) analytically and b) computationally.

Dimensionless parameter	Default value	Dimensionless parameter	Default value
Table 3. Default values of the dimensionless parameters used in the figures.			
ε	0.95	k	0.01 0.2 (Total Entropy)
Bi	1	k_{e1}	0.5
Br$'$	0.00001	k_{e2}	0.2
γ	0.5	Q	0.75
Da	0.1	Q_{w1}	0.5
Pe	10	Q_{w2}	0.2
Pr	5	ω	0.001
Re	75	φ	0.01
Sr	0.7	Y_1	0.9
ξ	0.05	Y_2	0.8